Mon. Not. R. Astron. Soc. **328,** 555–582 (2001)

An ultra-high-resolution study of the interstellar medium towards Orion

R. J. Price,★ I. A. Crawford, M. J. Barlow and I. D. Howarth
Department of Physics and Astronomy, University College London, Gower Street, London WC1E 6BT

Accepted 2001 August 6. Received 2001 August 6; in original form 2001 May 18

ABSTRACT

We report ultra-high-resolution observations ($R \approx 9 \times 10^5$) of Na I, Ca II, K I, CH and CH^+ for interstellar sightlines towards 12 bright stars in Orion. These data enable the detection of many more absorption components than previously recognized, providing a more accurate perspective on the absorbing medium. This is especially so for the line of sight to the Orion nebula, a region not previously studied at very high resolution. Model fits have been constructed for the absorption-line profiles, providing estimates for the column density, velocity dispersion and central velocity for each constituent velocity component. A comparison between the absorption occurring in sightlines with small angular separations has been used, along with comparisons with other studies, to estimate the line-of-sight velocity structures. Comparisons with earlier studies have also revealed temporal variability in the absorption-line profile of ζ Ori, highlighting the presence of small-scale spatial structure in the interstellar medium on scales of $\approx$10 au. Where absorption from both Na^0 and K^0 is observed for a particular cloud, a comparison of the velocity dispersions measured for each of these species provides rigorous limits on both the kinetic temperature and turbulent velocity prevailing in each cloud. Our results indicate the turbulent motions to be subsonic in each case. Na^0/Ca^+ abundance ratios are derived for individual clouds, providing an indication of their physical state.

Key words: line: profiles – ISM: atoms.

1 INTRODUCTION

The Orion region is well known for its ongoing star formation. The most active sites of star formation may be found on the western faces of the giant molecular clouds (GMCs) that form the backdrop of the constellation. In the model of the Orion region proposed by Cowie, Songaila & York (1979), the Orion OB1 association is located on the western side of the molecular-cloud complex, centred around the point where the Orion A and B GMCs meet. Using observations of CO, Bally et al. (1990) find the molecular gas located nearest to the centre of the association to exhibit the most positive radial velocities. These features are considered to be a result of shocks and ionizing radiation from association stars (Bally et al. 1990).

It is the influence of the association stars that is considered to produce the many loops and shell structures visible in this direction. In the model for the region proposed by Cowie et al. (1979), Barnard's Loop, which has the form of an incomplete elliptical ring centred on the OB1 association [not enclosing the λ Orionis association (Pickering 1890; Barnard 1895)], is interpreted as being an H II region at the inner edge of a dense shell of swept-up material. This is considered to be a part of the much larger Orion–Eridanus superbubble (Reynolds & Ogden 1979; Brown, Hartmann & Burton 1995; Heiles et al. 1999). Exterior to Barnard's Loop, Cowie et al. (1979) suggest the presence of a fast-moving (100 km s^{-1}), low-density shell centred on the Orion OB1 association, denoted 'Orion's cloak' because of the way in which it appears to cover the Hunter's back.

While the constellation's youngest stars reside beneath the surface of the molecular clouds, the youngest subgroup (Id; $<0.5 \times 10^6$ yr old; Warren & Hesser 1978) is present very near the surface, producing the Great Nebula in Orion (M42, NGC 1976, Orion A). The oldest of the stellar subgroups (Ia; $\approx 8 \times 10^6$ yr old; Warren & Hesser 1978) is located at the greatest distance from the parent molecular cloud.

The apparent brightness of the stars in Orion aids the spectroscopic study of the intervening interstellar (IS) matter. It was an investigation into the spectrum and orbit of δ Ori by Hartmann (1904) that led to the first identification of absorption arising in the interstellar medium (ISM). Subsequent observations of the H and K lines of Ca II by Beals (1936) revealed double and asymmetric components in the spectra of Orion stars, the first evidence pointing to the existence of multiple discrete IS clouds. These were the first steps in the study of a very complex IS sightline.

Earlier high-resolution surveys of matter in the ISM (e.g. Hobbs

★E-mail: rjp@star.ucl.ac.uk

1969a, hereafter H69; Hobbs 1969b,c, 1978b; Marschall & Hobbs 1972; Hobbs & Welty 1991; Welty, Hobbs & Kulkarni 1994, hereafter W94; Welty, Morton & Hobbs 1996, hereafter W96; Welty & Hobbs 2001, hereafter W01; detailed further in Section 4) have *included* observations of stars in the direction of Orion; however, none have concentrated on the ISM in this direction. The work of O'Dell et al. (1993, hereafter OD93), while focusing on the inner Orion nebula, utilized lower-resolution ($R \approx 9 \times 10^4$) Ca II K observations of the four Trapezium stars, and earlier Na I D_2 observations of Hobbs (1978b).

The aims of the current project are to obtain absorption-line profiles for the brighter Orion stars using spectra acquired with the Ultra-High-Resolution Facility (UHRF) at the Anglo-Australian Telescope. The resolving power of these data ($R \approx 9 \times 10^5$) exceeds all known previous observations of this region. Observations at such high spectral resolution enable many of the blended lines seen towards complex regions such as the Orion nebula (M42) to be resolved for the first time. These absorption components are then used to investigate the velocity structure of the Orion region, and the intervening ISM. Comparisons of absorption components found independently for Ca II, Na I and K I have been made in order to identify individual IS clouds producing recognizable absorption in one or more of these species. Where observations of closely spaced sightlines are available (i.e., the M42 region and λ Ori association), comparisons are also made between sightlines. This enables the identification of absorption systems, where absorption from individual IS clouds may be seen in more than one sightline. Where both Na I and K I line components are observed for a particular cloud, rigorous limits on both the kinetic temperature (T_k) and line-of-sight root-mean-square (rms) turbulent velocity (v_t) are derived (Section 5).

Following the identification of temporal variability in the IS absorption profile of δ Orionis (Price, Crawford & Barlow 2000, hereafter Paper I; Price, Crawford & Howarth 2001, hereafter Paper II), we compare current observations with those presented in previous studies, in order to identify any temporal variability present in other sightlines (Section 4).

2 OBSERVATIONS

The observations reported here were obtained using the UHRF on the 3.9-m Anglo-Australian Telescope. The majority of the observations were obtained during 1994 (January 20–23, and December 16–18 inclusive), with further observations made in 1996 (December 2), 1999 (January 29 and July 31) and 2000 (March 15). During 1994 January, a Thomson charge-coupled device (CCD) (1024×1024, 19-μm pixels) was used, while in 1999 January, the MITLL2 CCD (4096×2048, 15-μm pixels) was used. The remaining observations used a Tektronix CCD (1024×1024, 24-μm pixels). In all, 12 stars in Orion have been observed, including four in the M42 region. Table 1 lists the stars observed and relevant properties.

The spectrograph was operated with a confocal image slicer (Diego 1993), and the CCD output was binned (by factors of 4 or 8) perpendicular to the dispersion direction in order to reduce the readout noise. The instrument was operated in its highest resolution mode, providing a velocity resolution (as measured from the observed width of a stabilized He–Ne laser line) of $0.34 \pm 0.01\,\mathrm{km\,s^{-1}}$ full width at half-maximum (FWHM) ($R = 880\,000$) for all observations. Other aspects of the instrument and observing procedures have been described in detail by Diego et al. (1995) and Barlow et al. (1995).

Table 1. Stellar data, and a summary of UHRF exposures made for the targets observed in this study. Stellar positions have been obtained from Hoffleit & Jaschek (1982). Where available, *V* magnitudes and distances have been obtained from the *Hipparcos* and *Tycho* catalogues (ESA 1997). In the cases of θ^1 Ori A and C and θ^2 Ori A, distances are not available from the *Hipparcos* catalogue and have been taken from Goudis (1982). Spectral types have generally been obtained from Morgan, Code & Whitford (1955); in the case of λ Ori and θ^1 Ori A, Conti & Alschuler (1971) and Hoffleit & Jaschek (1982), respectively, have been used. Derivations of $E(B-V)$ have been made using the tabulations of Deutschman, Davis & Schild (1976), and data from Hoffleit & Jaschek (1982; θ^1 Ori A and C) and the *Hipparcos* and *Tycho* catalogues (ESA 1997; all other stars). Stellar heliocentric radial velocities ($v_\odot$) have been obtained from Wilson (1953) and Evans (1967). Columns 10–14 show the total exposure times in seconds, followed by the number of individual exposures, in parentheses; in the case of δ Ori, this only represents the 1994 observations.

Star	HD	l	b	V	Sp. type	$E(B-V)$	Dist.	$v_\odot$	Total exposure (s)				
		(°)	(°)				(pc)	($\mathrm{km\,s^{-1}}$)	Ca II K	Na I D_1	K I λ7698	CH λ4300	CH^+ λ4233
1	2	3	4	5	6	7	8	9	10	11	12	13	14
β Ori	34085	209 14	−25 15	0.28	B8Ia	−0.01	237^{+56}_{-38}	20.7 ± 0.9	2200(3)	3600(4)	200(1)	–	–
δ Ori	36486	203 52	−17 44	2.20	O9.5II	0.11	281^{+83}_{-53}	16.0 ± 2.0	1200(1)	3600(3)	–	–	–
ϕ^1 Ori	36822	195 24	−12 17	4.38	B0IV	0.16	302^{+57}_{-47}	33.2 ± 0.9	2400(2)	1800(1)	–	–	1200(1)
λ Ori	36861	195 03	−12 00	3.52	O8III	0.16	324^{+109}_{-66}	33.4 ± 0.5	2800(3)	1200(1)	–	–	1800(2)
θ^1 Ori A	37020	209 01	−19 23	4.98	O7	0.34	≈450	33.4 ± 2.0	5400(3)	–	–	–	–
θ^1 Ori C	37022	209 01	−19 23	5.13	O6	0.35	≈450	28.0 ± 5.0	5400(4)	2400(2)	–	3600(2)	2400(2)
θ^2 Ori A	37041	209 03	−19 22	4.98	O9.5V	0.22	≈450	35.6 ± 2.0	3600(2)	2250(1)	–	3600(2)	1200(1)
ι Ori	37043	209 31	−19 35	2.74	O9III	0.10	407^{+185}_{-97}	21.5 ± 0.9	3600(2)	3600(3)	–	–	–
ϵ Ori	37128	205 13	−17 14	1.69	B0Ia	0.07	412^{+246}_{-113}	25.9 ± 0.9	3000(3)	2000(2)	2400(2)	–	–
σ Ori	37468	206 49	−17 20	3.77	O9.5V	0.13	352^{+166}_{-85}	29.1 ± 2.0	3600(2)	1200(2)	–	–	–
ζ Ori	37742	206 27	−16 35	1.70	O9.5Ib	0.07	251^{+82}_{-42}	18.1 ± 0.9	3000(3)	3000(3)	2400(2)	–	–
κ Ori	38771	214 31	−18 30	2.04	B0.5Ia	0.06	221^{+46}_{-32}	20.5 ± 2.0	–	2400(2)	2400(2)	–	–

The spectra were extracted from the individual CCD images using the FIGARO data reduction package (Shortridge et al. 1999) at the UCL Starlink node. Scattered light and CCD dark current levels were measured from the inter-order region and subtracted. Wavelength calibration was performed using a Th–Ar lamp. An indication of the accuracy of this process for the Na I and Ca II regions may be obtained from the comparison of radial velocities of clouds producing well-determined absorption in both of these species (e.g., the detection of both Na I D_1 and Ca II K absorption, at velocities of 2.90 ± 0.01 and $2.88 \pm 0.01\,\mathrm{km\,s^{-1}}$, respectively, towards ϵ Ori). Furthermore, comparison of these data with previous studies has, in general, shown excellent agreement. However, in the case of six stars for which observations are presented here and in the Na I survey of W94, a small systematic velocity offset of $\approx -0.30 \pm 0.1\,\mathrm{km\,s^{-1}}$ is detected in the W94 data.

In the case of the K I λ7699 data, only two Th–Ar lines were found to occupy the spectral range of our observations, thus limiting our ability to calibrate wavelengths accurately for these data. A comparison of corresponding Na I and K I absorption components indicates there to be a velocity shift $\approx -0.3\,\mathrm{km\,s^{-1}}$ present in the K I spectra; however, the velocity shift is not constant over the spectral range. This has not been allowed for in the following analysis.

Continuum normalization has been achieved by division with low-order polynomial fits to the continuum; however, in the case of β Ori, the presence of strong stellar Ca II absorption has created some uncertainty with this procedure, resulting in the use of a manually drawn continuum. A typical spectral range of $\approx 130\,\mathrm{km\,s^{-1}}$ was obtained, which in general is centred on the IS absorption. In the case of the Ca II observations of θ^1 Ori A and C and θ^2 Ori A, a lack of well-determined red-wing continuum does lead to some uncertainty in the normalization process; however, the requirement of only first- and second-order polynomial fits to the (blue) continuum alleviates this uncertainty. Removal of telluric (water) lines from the Na I and K I spectra has been achieved by division by atmospheric template spectra, observed towards the bright, lightly reddened star α Vir [note that α Vir actually exhibits a single weak Na I absorption component at a velocity of $-11.2\,\mathrm{km\,s^{-1}}$ (Welsh, Vedder & Vallerga 1990), but this is clear of all absorption components observed towards the stars in this study]. These atmospheric templates were acquired with the same instrument during observing runs in 1994 (Na I) and 1993 (K I). To account for small variations in the strengths of the atmospheric lines between the different spectra, the optical depth of the adopted atmospheric template was scaled before division. The spectra were converted to a heliocentric velocity frame and individual exposures of the same star/transition were added (the number of individual observations comprising each spectrum is shown in parentheses after the total exposure times in Table 1). All velocities referred to here are heliocentric unless otherwise stated.

During the analysis of the data, a small discrepancy in the zero level was found in the cores of saturated Na I D_1 lines towards λ and ϕ^1 Ori. The lines were seen to reach 0.01 and 0.02 of the continuum, respectively; therefore the zero level of the two spectra were readjusted. This provides a guide to the likely uncertainty in the zero level of the remaining (uncorrected) Na I spectra. Since fully saturated interstellar Ca II K lines have never been observed, it is not possible to assess the zero-level error for the Ca II region in this manner; however, the excellent agreement seen between these observations and those presented in other studies (see Section 4) suggests zero-level errors in the Ca II region to be minor (i.e. of the order 1–2 per cent).

3 LINE-PROFILE ANALYSIS

The absorption lines were initially modelled using the IS line fitting routines in the DIPSO spectral analysis program (Howarth, Murray & Mills 1993). These models were subsequently optimized through the use of the VAPID line fitting routine (Howarth et al. in preparation), which evaluates the set of component parameters that produce the minimum rms residuals. During the fitting procedure, all component parameters were unconstrained. The number of components employed in each model was kept to a minimum, such that any additional components did not provide a significant statistical improvement to the fit (with the exception of the K I model of κ Ori, discussed in Section 5.4). In a small number of cases this has resulted in the inclusion of very broad components which, statistically, cannot be replaced by multiple, narrower components (ζ Ori Ca II, $v_\odot = 23.74$; σ Ori Ca II, $v_\odot = 10.25$; λ Ori Na I, $v_\odot = 30.74$). Nevertheless, we feel that the use of unconstrained model parameters is preferable since, although the Ca II, Na I and K I models have been independently generated, the generally good agreement between the Ca II, Na I and K I absorption model components suggests that the majority of the individual clouds have been identified. Furthermore, it has been possible to model simultaneously the various spectra for a given star. Where a cloud is identified in both Na I and Ca II, its velocity can be constrained to be equal in both species, but remain variable to optimize the fit. Simultaneous absorption models were generated for a selection of stars but show little, if any, variation with those generated independently. In fact, our results show that Ca^+ is generally present in warmer regions of the cloud than Na^0, therefore providing no reason to force the Ca II and Na I absorption to occur at exactly the same velocity. In the case of Na^0 and K^0 where there are good reasons to assume the species to be co-spatial, and therefore to model them simultaneously, the variable velocity offset detected in the K I spectra (Section 2) makes the procedure impracticable.

By reconstructing the absorption models presented in the high-resolution, high-S/N (signal-to-noise ratio) surveys conducted by W94 (Na I), W96 (Ca II) and W01 (K I), it becomes possible to compare their exact component structures with those now derived here. In the case of Ca II we find that, with the exception of θ^1 Ori C, towards which we identify significant additional structure, the higher S/N achieved by W96 in their Ca II observations has in general allowed the use of a greater number of components. In a small number of cases, our use of fully unconstrained parameters in the modelling process has led to the inclusion of very broad components (ζ Ori, $v_\odot = 23.74$; σ Ori, $v_\odot = 10.25$) not seen in the W96 models. In general, very good agreement is present between the Na I component structures modelled here and by W94. The higher resolution employed by us typically enables additional substructure to be resolved, while the higher S/N that we have achieved allows us to identify additional weak components. In the case of the K I observations, there is good agreement between the column densities found here and those of W01. The higher S/N achieved by W01 in their K I observation of ϵ Ori makes possible the detection of a weak component at a velocity of $17.17\,\mathrm{km\,s^{-1}}$ (corresponding to our cloud 8 towards this star). The higher resolution employed here has, in the case of ζ Ori, resolved three additional components, while for κ Ori, further substructure is suggested in the spectrum and, although not statistically significant, has been modelled on the grounds of our Na I observations (see Section 5.4).

The atomic data adopted for the various transitions are listed in

Table 2. Wavelengths (λ) and corresponding oscillator strengths (f) adopted for the line-profile analyses. Hyperfine splitting of the Na I D_1 and K I λ7699 transitions has been accounted for in the modelling process. The information is taken from: (1) Morton (1991); (2) Black & van Dishoeck (1988); and (3) Lambert & Danks (1986).

Line	λ (Å)	f	Ref.
Ca II K	3933.663	0.635	(1)
Na I D_1	5895.9108	0.119	(1)
	5895.9321	0.199	(1)
K I	7698.969	0.127	(1)
	7698.978	0.212	(1)
CH $R_2(1)$	4300.313	0.0051	(2)
CH^+ R(0)	4232.548	0.0055	(3)

Table 2. The resulting line-profile parameters, heliocentric radial velocity, $v_\odot$, velocity dispersion, b, and column density, N, are listed in Table 3, along with the 1σ, single-parameter errors. In the case of Na I and K I, $v_\odot$ corresponds to the weighted mean velocity of the two hyperfine split (HFS; discussed further below) components. The corresponding best-fitting model profiles, after convolution with the instrumental response function, are shown in Fig. 1, overplotted on the observed line profiles.

The hyperfine splitting of the Na I D_1 and K I λ7699 lines (amounting to a separation of 1.08 km s^{-1}, or 21 mÅ, in the case of Na I D_1; and to 0.35 km s^{-1}, or 9 mÅ, in the case of K I λ7699) has been accounted for in the modelling of these transitions (see Table 2). The ability of the UHRF to resolve distinctly the HFS of narrow (and not strongly blended) Na I D_1 components places rigorous limits on the range of permitted b values. Furthermore, the UHRF is capable of resolving intrinsic linewidths for components with b values as low as 0.2 km s^{-1} (which, in the case of Na, corresponds to a cloud with $T_k = 50$ K, and $v_t = 0.05$ km s^{-1}). Many examples of resolved HFS components are visible in Fig. 1, a notable example being the 2.90 km s^{-1} component observed towards ϵ Ori, which has a derived b value of 0.35 km s^{-1} (discussed in Section 5). However, even at the resolution employed here we still find regions of closely blended components that cannot be unambiguously disentangled. Indeed, many components present in regions of velocity space containing significant amounts of substructure may remain unidentified, irrespective of the resolution employed.

Where observations of more than one atom/ion are available for a given star, the comparison of absorption *components* present in each waveband enables the identification of individual IS *clouds* (numbered according to radial velocity in Table 3). Furthermore, where observations of stars with small angular separations are available, it is possible to identify absorption *systems*, whereby individual IS clouds produce absorption (characterized by components with similar parameters) in more than one sightline. The identification of these absorption *systems* will be made in Sections 7.1 (for the M42 region) and 7.2 (for the λ Ori association). The absorption *systems* are numbered according to velocity, but during the discussion of Sections 7.1 and 7.2 the *systems* will be referred to by either an M or λ (denoting M42 and λ Ori regions respectively) followed by a bold number, so as to reduce confusion with individual clouds.

Observations of CH λ4300 and/or CH^+ λ4233 have been made towards a number of our targets; however, no absorption components have been positively identified in any of these spectra. Table 4 lists the S/N and upper limits to the equivalent widths (W_λ) and column density of any absorption present in each of these spectra. In general, these values represent better limits than those determined in previous studies (e.g. Hobbs 1973; Federman 1982; Lambert & Danks 1986).

4 SEARCH FOR TEMPORAL VARIABILITY

Previous observations of IS absorption towards the stars observed here have been made at a variety of resolutions, and include the studies by H69, Marschall & Hobbs (1972), OD93, W94, W96 and W01. The resolving power achieved by the UHRF exceeds that of these earlier observations, although the Na I survey of W94 did employ a comparable resolving power ($R = 6 \times 10^5$), while the W96 Ca II survey (conducted mainly with a resolving power of $R = 2.5 \times 10^5$) included two UHRF observations of stars also observed here. H69 estimated the resolving power of the PEPSIOS Fabry–Perot interferometer to be approximately 6×10^5, although a comparison between PEPSIOS and UHRF observations (Barlow et al. 1995) suggested that the resolving power of the former was probably in the range $R \approx (1\text{–}2) \times 10^5$. For the purposes of comparison, we here assume a value of $R = 2 \times 10^5$ for the PEPSIOS data.

Following the discovery of temporal variability in the IS spectra of δ Orionis (Papers I and II), an examination of the remaining spectra has been made in order to identify any variability in other sightlines. Comparisons have primarily been made with the studies by OD93, W94, W96 and W01, for which absorption models have been published, while additional comparisons have also been made with the observations by H69 and Marschall & Hobbs (1972). However, the presence of telluric absorption in the Na I spectra by H69 limits our ability to identify confidently temporal variability. By reconstructing the relevant absorption models presented by OD93, W94, W96 and W01, it became easier to compare their observations with ours.

During these comparisons the resolution of our observations was degraded (through Gaussian convolution) to a level equal to that of the observations with which the comparison was being made. In this way, we hope that any changes found cannot be ascribed to the different resolving powers employed. Several examples of possible variability have been found. These are displayed in Fig. 2 and are discussed individually below. Similar investigations carried out by W94 and W96 found no evidence for temporal variability; however, the success of our investigation is primarily due to the availability of the observations made by W94 and W96. In hindsight, subtle variations can also be seen between the observations by W94 and by H69, and between those of W96 and Marschall & Hobbs (1972). The small discrepancy in velocity scales found between our data and those of W94 (noted in Section 2) has been allowed for through the application of small velocity shifts to the W94 data, in order to achieve maximum agreement between data sets.

4.1 δ Orionis

Striking line-profile variations have been detected towards δ Ori A, attributed to the passage of an IS cloud, most likely present within the expanding H I shell surrounding the Orion–Eridanus superbubble. The line-profile variability seen towards δ Ori A is discussed in detail in Papers I and II. In the latter paper, absorption-line profile differences between δ Ori A and δ Ori C are also reported,

Table 3. Component parameters derived from the absorption-line modelling for the Orion stars. For each velocity component, values of $v_\odot$ (heliocentric radial velocity), b (velocity dispersion) and N (column density) are shown in columns 2–4 (for Ca^+), 6–8 (for Na^0) and 9–11 (for K^0). Achieved S/N ratios and total equivalent widths (W_λ) are displayed alongside each star's identifier. In the case of both Na I and K I absorption, central velocities are with respect to the weighted mean of the two hyperfine split components. Where Ca II and/or Na I and/or K I components (towards a given star) appear in the same row, and are hence identified by the same cloud number (column 1), the absorption is considered to occur in the same individual interstellar cloud. Column 5 gives cloud Na^0/Ca^+ ratios. Where multiple entries are made with a single cloud number (towards a given star), absorption is considered to arise in multiple unresolved clouds and an average Na^0/Ca^+ ratio is obtained from the summed Na^0 and Ca^+ column densities. Where a Na I component possesses no Ca II counterpart, a 2σ upper limit to the undetected Ca^+ column density is derived (see Section 6) and a lower limit to the Na^0/Ca^+ ratio is obtained; in the reverse situation, an upper limit is obtained. Systems undergoing possible temporal variability (discussed in Section 4) are identified in column 1 with a superscript '†'. In the case of δ Ori, also see Papers I and II.

	Ca II K				Na I D_1			K I λ7699		
Star/ cloud	$v_\odot$ (km s^{-1})	b (km s^{-1})	log N (cm^{-2})	$\frac{Na^0}{Ca^+}$	$v_\odot$ (km s^{-1})	b (km s^{-1})	log N (cm^{-2})	$v_\odot$ (km s^{-1})	b (km s^{-1})	log N (cm^{-2})
1	2	3	4	5	6	7	8	9	10	11
ϵ Ori	S/N = 114; W_λ = 85.4 ± 0.3 mÅ				S/N = 192; W_λ = 156.6 ± 0.1 mÅ			S/N = 127; W_λ = 2.7 ± 0.3 mÅ		
1	1.17 ± 0.82	3.47 ± 0.62	10.84 ± 0.13	<0.04						
2	2.88 ± 0.01	0.31 ± 0.02	10.61 ± 0.02	1.78	2.90 ± 0.01	0.35 ± 0.01	10.86 ± 0.02			
3	4.82 ± 0.13	2.02 ± 0.37	10.87 ± 0.14	1.78	4.76 ± 0.29	2.89 ± 0.22	11.12 ± 0.04			
4a	7.90 ± 0.21	1.06 ± 0.30	10.49 ± 0.19	2.29	9.61 ± 0.47	2.03 ± 0.61	11.10 ± 0.18			
4b	9.19 ± 0.08	0.60 ± 0.14	10.37 ± 0.27							
5	10.88 ± 0.02	0.86 ± 0.13	11.09 ± 0.21	2.63	10.94 ± 0.01	0.63 ± 0.02	11.51 ± 0.03	10.55 ± 0.04	0.54 ± 0.07	9.87 ± 0.04
6	12.41 ± 0.02	0.36 ± 0.07	10.33 ± 0.13	6.76	12.35 ± 0.02	0.75 ± 0.04	11.16 ± 0.05			
7a	12.50 ± 0.97	2.24 ± 0.92	11.15 ± 0.28	0.54	13.67 ± 0.04	0.17 ± 0.10	9.86 ± 0.11			
7b					14.74 ± 0.02	0.59 ± 0.03	10.84 ± 0.02			
8	17.26 ± 0.03	0.59 ± 0.06	10.41 ± 0.07	5.62	17.18 ± 0.01	0.47 ± 0.01	11.16 ± 0.02			
9	18.31 ± 0.19	2.50 ± 0.24	11.06 ± 0.05	0.81	17.49 ± 0.07	1.50 ± 0.09	10.97 ± 0.04			
10a	23.84 ± 0.71	1.65 ± 0.48	10.85 ± 0.26	3.09	22.70 ± 0.02	0.70 ± 0.03	11.17 ± 0.01			
10b					23.79 ± 0.02	0.35 ± 0.03	10.86 ± 0.06			
11	25.07 ± 0.04	0.87 ± 0.12	11.06 ± 0.16	4.57	24.77 ± 0.01	0.58 ± 0.02	11.72 ± 0.02	24.70 ± 0.04	0.56 ± 0.07	9.87 ± 0.04
12	26.22 ± 0.08	0.53 ± 0.10	10.40 ± 0.15	9.55	26.01 ± 0.05	0.93 ± 0.07	11.38 ± 0.04			
13	28.01 ± 0.02	1.36 ± 0.03	11.36 ± 0.01	0.41	28.17 ± 0.05	0.81 ± 0.06	10.97 ± 0.04			
14				>11.75	29.89 ± 0.20	0.91 ± 0.24	10.39 ± 0.10			
15	37.05 ± 0.26	3.69 ± 0.37	10.48 ± 0.04	<0.09						
ζ Ori	S/N = 111; W_λ = 79.7 ± 0.3 mÅ				S/N = 156; W_λ = 150.7 ± 0.3 mÅ			S/N = 116; W_λ = 5.0 ± 0.2 mÅ		
1	−8.56 ± 0.39	1.84 ± 0.37	10.29 ± 0.12	<0.11						
2a	−5.05 ± 0.14	1.75 ± 0.17	11.09 ± 0.08	1.40	−6.05 ± 0.07	0.69 ± 0.11	10.32 ± 0.07			
2b	−1.85 ± 0.16	2.07 ± 0.46	11.12 ± 0.15		−3.05 ± 0.06	0.44 ± 0.11	10.13 ± 0.14			
2c	1.85 ± 0.88	2.33 ± 1.51	10.62 ± 0.37		−2.23 ± 0.06	3.43 ± 0.10	11.43 ± 0.01			
2d					−2.06 ± 0.03	0.26 ± 0.07	10.22 ± 0.06			
2e†					−1.07 ± 0.01	0.44 ± 0.02	10.98 ± 0.02	−1.31 ± 0.06	0.04 ± 0.42	9.31 ± 0.13
3a	6.27 ± 0.37	1.92 ± 0.93	10.43 ± 0.29	0.76	8.27 ± 1.17	2.51 ± 0.58	10.82 ± 0.38			
3b	9.88 ± 0.18	1.84 ± 0.48	10.78 ± 0.16							
4	11.43 ± 0.06	0.38 ± 0.14	9.70 ± 0.19	4.27	11.50 ± 0.02	0.38 ± 0.04	10.33 ± 0.06			
5	13.70 ± 0.22	2.36 ± 0.52	10.89 ± 0.13	1.29	11.63 ± 1.05	2.76 ± 0.65	11.00 ± 0.26			
6†	18.39 ± 0.22	0.95 ± 0.16	10.68 ± 0.26	0.96	18.11 ± 0.03	0.62 ± 0.05	10.66 ± 0.05			
7a	19.98 ± 0.51	1.17 ± 0.80	10.52 ± 0.34	1.48	19.46 ± 0.19	1.98 ± 0.20	10.83 ± 0.04			
7b	21.55 ± 0.08	0.52 ± 0.17	10.10 ± 0.32							
8a	23.06 ± 0.05	0.84 ± 0.05	11.17 ± 0.08	6.03	22.97 ± 0.01	0.32 ± 0.02	11.19 ± 0.06	22.97 ± 0.04	0.44 ± 0.06	10.13 ± 0.04

Table 3 – *continued*

Star/ cloud	Ca II K $v_\odot$ (km s^{-1})	Ca II K b (km s^{-1})	Ca II K log N (cm^{-2})	$\frac{Na^0}{Ca^+}$	Na I D_1 $v_\odot$ (km s^{-1})	Na I D_1 b (km s^{-1})	Na I D_1 log N (cm^{-2})	K I λ7699 $v_\odot$ (km s^{-1})	K I λ7699 b (km s^{-1})	K I λ7699 log N (cm^{-2})
1	2	3	4	5	6	7	8	9	10	11
8b					23.19 ± 0.01	0.82 ± 0.02	11.87 ± 0.01	23.80 ± 0.16	0.16 ± 0.39	9.20 ± 0.30
9	23.74 ± 1.61	5.69 ± 0.88	11.10 ± 0.18	<0.03						
10	24.59 ± 0.20	1.21 ± 0.30	10.96 ± 0.13	1.51	25.08 ± 0.03	0.51 ± 0.04	11.14 ± 0.06			
11a	26.35 ± 0.01	0.52 ± 0.02	10.77 ± 0.04	11.48	26.20 ± 0.01	0.24 ± 0.03	11.09 ± 0.05	25.71 ± 2.01	0.58 ± 0.94	9.60 ± 1.86
11b					26.41 ± 0.03	0.76 ± 0.02	11.74 ± 0.02	26.24 ± 0.13	0.31 ± 0.32	9.94 ± 0.84
12	37.00 ± 0.09	1.96 ± 0.12	10.45 ± 0.02	<0.08						
1994										
δ Ori	S/N = 14; W_λ = 36.1 ± 2.0 mÅ				S/N = 185; W_λ = 60.8 ± 0.2 mÅ					
1				>0.45	−4.92 ± 0.12	0.83 ± 0.23	9.86 ± 0.06			
2				>0.85	0.03 ± 0.34	2.44 ± 0.46	10.37 ± 0.08			
3				>1.29	4.72 ± 0.20	2.12 ± 0.43	10.52 ± 0.11			
4	10.07 ± 1.05	7.63 ± 1.31	11.31 ± 0.07	0.45	9.32 ± 0.12	2.63 ± 0.18	10.96 ± 0.03			
5	15.77 ± 0.31	1.26 ± 0.57	10.50 ± 0.22	1.51	15.07 ± 0.04	1.56 ± 0.07	10.68 ± 0.01			
6†	21.23 ± 0.05	0.74 ± 0.07	11.07 ± 0.04	0.74	21.25 ± 0.01	0.45 ± 0.01	10.94 ± 0.02			
7a	23.63 ± 0.25	1.13 ± 0.42	10.59 ± 0.13	7.08	22.56 ± 0.53	2.41 ± 0.33	11.12 ± 0.11			
7b					24.85 ± 0.07	1.38 ± 0.15	11.16 ± 0.10			
8				>5.13	25.11 ± 0.01	0.36 ± 0.02	10.74 ± 0.04			
9				>3.16	26.57 ± 0.01	0.38 ± 0.03	10.54 ± 0.04			
10	28.56 ± 0.48	2.59 ± 0.74	10.79 ± 0.10	<0.04						
1999										
δ Ori					S/N = 31; W_λ = 60.3 ± 1.4 mÅ					
6†					21.26 ± 0.07	0.44 ± 0.09	10.60 ± 0.05			
2000										
δ Ori					S/N = 82; W_λ = 52.1 ± 0.7 mÅ					
6†					21.39 ± 0.05	0.39 ± 0.06	10.24 ± 0.04			
σ Ori	S/N = 43; W_λ = 91.0 ± 1.0 mÅ				S/N = 114; W_λ = 154.7 ± 0.5 mÅ					
1	−10.85 ± 0.27	3.45 ± 0.40	10.75 ± 0.04	<0.07						
2	−0.34 ± 0.21	3.09 ± 0.29	11.30 ± 0.10	0.58	−0.12 ± 0.17	3.04 ± 0.20	11.07 ± 0.03			
3a	5.37 ± 0.13	1.44 ± 0.36	10.60 ± 0.22	1.00	6.20 ± 0.15	2.79 ± 0.38	11.07 ± 0.05			
3b	7.64 ± 0.20	0.54 ± 0.34	9.80 ± 0.29		9.75 ± 0.39	1.00 ± 0.74	10.13 ± 0.39			
3c	10.25 ± 2.35	7.54 ± 7.26	11.06 ± 0.40		12.57 ± 0.39	1.86 ± 0.55	10.52 ± 0.11			
4	15.57 ± 0.09	0.82 ± 0.19	10.40 ± 0.15	<0.08						
5	17.34 ± 0.10	0.50 ± 0.18	10.08 ± 0.18	1.55	16.66 ± 0.08	0.47 ± 0.07	10.28 ± 0.05			
6a				6.92	18.56 ± 0.04	0.43 ± 0.05	10.85 ± 0.08			
6b	19.65 ± 0.03	0.55 ± 0.07	10.76 ± 0.10		19.64 ± 0.01	0.62 ± 0.03	11.92 ± 0.07			
6c	20.15 ± 0.17	1.67 ± 0.24	11.16 ± 0.07		20.61 ± 0.23	1.16 ± 0.19	11.71 ± 0.11			
7a	24.42 ± 0.08	1.27 ± 0.24	11.47 ± 0.40	2.96	23.85 ± 0.01	0.67 ± 0.01	11.99 ± 0.01			
7b	24.98 ± 0.03	0.22 ± 0.06	10.53 ± 0.07		24.88 ± 0.04	0.53 ± 0.06	11.27 ± 0.14			

Table 3 – *continued*

Star/ cloud	Ca II K $v_\odot$ (km s^{-1})	Ca II K b (km s^{-1})	Ca II K log N (cm^{-2})	$\frac{Na^0}{Ca^+}$	Na I D$_1$ $v_\odot$ (km s^{-1})	Na I D$_1$ b (km s^{-1})	Na I D$_1$ log N (cm^{-2})	K I λ7699 $v_\odot$ (km s^{-1})	K I λ7699 b (km s^{-1})	K I λ7699 log N (cm^{-2})
1	2	3	4	5	6	7	8	9	10	11
7c	25.74 ± 2.43	1.97 ± 1.54	11.16 ± 0.87		25.64 ± 0.24	1.13 ± 0.17	11.37 ± 0.11			
8	30.06 ± 1.01	2.75 ± 1.55	10.71 ± 0.28	<0.07						
9	37.33 ± 0.78	3.12 ± 1.58	10.72 ± 0.21	<0.08						
10	40.80 ± 0.21	1.37 ± 0.46	10.42 ± 0.30	<0.10						
θ^1 Ori A	S/N = 17; W_λ = 119.2 ± 1.9 mÅ									
1	0.27 ± 0.73	2.18 ± 0.75	10.85 ± 0.29							
2	5.93 ± 0.68	3.64 ± 2.22	11.27 ± 0.24							
3	10.20 ± 0.10	1.57 ± 0.23	11.38 ± 0.12							
4	13.19 ± 0.11	0.98 ± 0.18	10.95 ± 0.08							
5	16.56 ± 0.17	1.68 ± 0.34	11.20 ± 0.07							
6	18.86 ± 0.21	0.75 ± 0.35	10.73 ± 0.47							
7	20.69 ± 0.89	1.49 ± 2.46	10.72 ± 0.66							
8	23.21 ± 0.22	0.97 ± 0.52	10.99 ± 0.72							
9	24.96 ± 2.57	1.88 ± 4.00	10.90 ± 1.13							
10	29.48 ± 0.45	2.03 ± 1.26	11.29 ± 0.28							
11	31.91 ± 0.10	1.09 ± 0.15	11.37 ± 0.15							
12	36.77 ± 0.46	1.95 ± 0.75	10.68 ± 0.14							
13	40.60 ± 0.28	1.39 ± 0.41	10.70 ± 0.12							
14	46.87 ± 0.37	2.16 ± 0.53	10.73 ± 0.09							
θ^1 Ori C	S/N = 32; W_λ = 120.7 ± 1.2 mÅ				S/N = 71; W_λ = 172.2 ± 0.8 mÅ					
1	−1.42 ± 0.26	1.73 ± 0.39	10.48 ± 0.09	1.78	0.00 ± 2.65	3.46 ± 1.83	10.73 ± 0.44			
2	1.19 ± 0.07	0.36 ± 0.12	10.14 ± 0.11	1.12	1.60 ± 0.20	0.69 ± 0.34	10.19 ± 0.25			
3	6.42 ± 0.14	4.07 ± 0.27	11.48 ± 0.02	0.91	6.28 ± 0.31	3.41 ± 0.93	11.44 ± 0.13			
4a	9.97 ± 0.13	0.53 ± 0.20	10.24 ± 0.24	1.15	10.38 ± 0.28	1.62 ± 0.79	10.75 ± 0.36			
4b	11.67 ± 0.33	1.14 ± 0.82	10.50 ± 0.30							
5	13.86 ± 0.28	1.02 ± 0.58	10.57 ± 0.39	0.98	13.84 ± 0.33	1.43 ± 0.93	10.56 ± 0.22			
6	16.45 ± 0.17	1.68 ± 0.68	11.08 ± 0.16	0.89	16.44 ± 0.08	0.76 ± 0.08	11.03 ± 0.03			
7	18.49 ± 0.14	0.71 ± 0.28	10.50 ± 0.33	21.38	18.66 ± 0.03	0.77 ± 0.02	11.83 ± 0.02			
8	20.46 ± 0.06	1.10 ± 0.18	11.13 ± 0.13	5.13	20.55 ± 0.04	1.18 ± 0.06	11.84 ± 0.02			
9	23.47 ± 0.09	0.77 ± 0.17	10.70 ± 0.17	7.24	23.46 ± 0.02	0.77 ± 0.03	11.56 ± 0.02			
10	23.99 ± 0.71	3.36 ± 1.62	11.31 ± 0.19	0.63	25.42 ± 0.17	1.43 ± 0.18	11.11 ± 0.05			
11	30.19 ± 0.07	0.68 ± 0.19	10.72 ± 0.29	0.56	30.07 ± 0.05	0.47 ± 0.06	10.47 ± 0.05			
12	30.46 ± 0.71	2.70 ± 0.75	11.40 ± 0.09	<0.02						
13	32.23 ± 0.05	0.89 ± 0.09	11.29 ± 0.10	0.69	32.17 ± 0.03	1.00 ± 0.06	11.13 ± 0.01			
14	35.59 ± 0.33	1.01 ± 0.60	10.16 ± 0.37	<0.25						
15	39.68 ± 0.39	4.44 ± 0.89	11.19 ± 0.07	<0.05						
16	46.39 ± 0.30	1.64 ± 0.48	10.42 ± 0.16	<0.17						
θ^2 Ori A	S/N = 59; W_λ = 101.4 ± 0.7 mÅ				S/N = 33; W_λ = 184.0 ± 1.6 mÅ					
1a	−1.89 ± 0.46	3.01 ± 0.35	11.18 ± 0.09	1.20	−3.87 ± 0.40	0.96 ± 0.87	10.30 ± 0.29			
1b	2.39 ± 0.27	2.48 ± 0.47	11.13 ± 0.15		1.89 ± 0.20	4.31 ± 0.46	11.51 ± 0.03			
2	8.49 ± 0.68	3.67 ± 2.50	10.90 ± 0.28	0.62	8.44 ± 0.33	1.18 ± 0.63	10.69 ± 0.17			

Table 3 – *continued*

Star/ cloud	Ca II K $v_\odot$ (km s^{-1})	Ca II K b (km s^{-1})	Ca II K log N (cm^{-2})	$\frac{Na^0}{Ca^+}$	Na I D_1 $v_\odot$ (km s^{-1})	Na I D_1 b (km s^{-1})	Na I D_1 log N (cm^{-2})	K I λ7699 $v_\odot$ (km s^{-1})	K I λ7699 b (km s^{-1})	K I λ7699 log N (cm^{-2})
1	2	3	4	5	6	7	8	9	10	11
3	11.01 ± 0.08	0.76 ± 0.19	10.37 ± 0.19	7.08	11.02 ± 0.08	0.78 ± 0.11	11.22 ± 0.04			
4	14.51 ± 0.25	1.96 ± 0.47	11.00 ± 0.15	3.02	14.78 ± 0.07	1.89 ± 0.15	11.48 ± 0.02			
5	17.10 ± 0.23	1.21 ± 0.32	10.55 ± 0.22	2.14	18.14 ± 0.06	0.44 ± 0.06	10.88 ± 0.07			
6	19.88 ± 0.01	0.90 ± 0.02	11.38 ± 0.01	4.79	20.08 ± 0.02	0.74 ± 0.03	12.06 ± 0.01			
7	23.19 ± 0.08	2.52 ± 0.21	11.24 ± 0.03	3.39	23.21 ± 0.11	2.68 ± 0.19	11.77 ± 0.03			
8	26.10 ± 0.04	0.44 ± 0.07	10.34 ± 0.07	2.09	26.20 ± 0.03	0.22 ± 0.07	10.66 ± 0.09			
9	29.35 ± 0.06	2.19 ± 0.12	11.30 ± 0.02	<0.06						
10	32.27 ± 0.02	0.84 ± 0.04	11.00 ± 0.03	0.78	32.30 ± 0.08	0.79 ± 0.15	10.89 ± 0.04			
11	36.39 ± 0.34	2.62 ± 0.55	10.71 ± 0.09	<0.25						
12	40.80 ± 0.17	0.86 ± 0.42	10.05 ± 0.37	<0.65						
13	42.80 ± 1.57	2.94 ± 1.59	10.43 ± 0.29	<0.49						
ι Ori	S/N = 87; W_λ = 45.5 ± 0.4 mÅ				S/N = 110; W_λ = 46.0 ± 0.4 mÅ					
1				>9.12	0.91 ± 0.13	2.58 ± 0.19	10.62 ± 0.03			
2a	8.34 ± 0.02	0.67 ± 0.03	10.96 ± 0.02	1.95	8.13 ± 0.16	0.56 ± 0.08	10.97 ± 0.16			
2b					8.72 ± 0.05	0.38 ± 0.07	10.93 ± 0.18			
3	9.70 ± 0.20	0.64 ± 0.33	9.93 ± 0.22	2.14	9.86 ± 0.12	0.67 ± 0.19	10.26 ± 0.08			
4	12.10 ± 0.26	1.47 ± 0.42	10.12 ± 0.10	0.72	12.63 ± 0.09	0.49 ± 0.10	9.98 ± 0.06			
5				>15.49	23.74 ± 0.15	0.77 ± 0.12	10.59 ± 0.11			
6	25.27 ± 0.07	1.47 ± 0.08	10.92 ± 0.04	0.93	25.26 ± 0.07	0.86 ± 0.17	10.89 ± 0.08			
7				>7.24	26.43 ± 0.06	0.37 ± 0.13	10.10 ± 0.21			
8	28.81 ± 0.11	2.41 ± 0.20	11.10 ± 0.03	<0.03						
9	33.33 ± 0.01	1.21 ± 0.02	11.45 ± 0.01	0.26	33.66 ± 0.02	0.87 ± 0.04	10.87 ± 0.01			
10	40.42 ± 0.11	1.12 ± 0.16	10.22 ± 0.05	<0.15						
λ Ori	S/N = 98; W_λ = 194.0 ± 0.4 mÅ				S/N = 51; W_λ = 240.2 ± 0.9 mÅ					
1	−18.51 ± 0.31	2.24 ± 0.45	10.11 ± 0.07	<0.58						
2	−9.54 ± 0.15	4.01 ± 0.26	10.92 ± 0.02	<0.12						
3	−5.54 ± 0.12	0.38 ± 0.21	9.45 ± 0.20	<1.10						
4	−1.83 ± 0.17	2.48 ± 0.22	10.96 ± 0.05	<0.09						
5	4.01 ± 1.24	2.74 ± 0.97	11.15 ± 0.32	<0.06						
6a	7.32 ± 0.09	2.24 ± 0.13	11.94 ± 0.06	0.20	7.28 ± 3.20	2.51 ± 2.02	10.95 ± 0.70			
6b					8.47 ± 0.14	0.79 ± 0.33	10.93 ± 0.40			
7	9.41 ± 0.04	0.15 ± 0.09	9.83 ± 0.10	4.37	9.68 ± 0.06	0.29 ± 0.16	10.47 ± 0.29			
8	10.71 ± 0.31	1.72 ± 0.39	10.83 ± 0.20	0.71	10.81 ± 0.68	1.08 ± 1.00	10.68 ± 0.62			
9	15.53 ± 0.04	2.71 ± 0.11	11.70 ± 0.02	0.96	16.23 ± 0.31	3.67 ± 0.61	11.68 ± 0.07			
10	18.18 ± 0.09	0.89 ± 0.12	10.79 ± 0.18	0.35	18.52 ± 0.20	0.43 ± 0.28	10.34 ± 0.42			
11	20.41 ± 0.17	1.61 ± 0.47	11.31 ± 0.13	0.15	19.62 ± 0.27	0.56 ± 0.37	10.48 ± 0.38			
12a	21.62 ± 0.04	0.51 ± 0.11	10.63 ± 0.22	13.49	22.86 ± 0.60	1.46 ± 0.42	12.08 ± 0.27			
12b	22.40 ± 0.04	0.24 ± 0.09	10.16 ± 0.20		26.02 ± 0.12	1.76 ± 0.08	13.18 ± 0.05			
12c	23.77 ± 0.13	1.34 ± 0.20	11.70 ± 0.09							
12d	25.48 ± 0.08	0.91 ± 0.23	11.29 ± 0.23							
12e	26.55 ± 0.02	0.54 ± 0.03	11.39 ± 0.07							
12f	27.64 ± 0.07	1.03 ± 0.09	11.32 ± 0.05							
13	29.83 ± 0.09	0.76 ± 0.15	10.28 ± 0.13	1.95	31.06 ± 0.31	1.01 ± 0.58	10.57 ± 0.16			
14	30.74 ± 2.41	5.28 ± 1.90	10.70 ± 0.25	0.93	35.59 ± 0.38	2.25 ± 0.64	10.67 ± 0.09			

Table 3 – *continued*

Star/ cloud	Ca II K $v_\odot$ (km s^{-1})	Ca II K b (km s^{-1})	Ca II K log N (cm^{-2})	$\frac{Na^0}{Ca^+}$	Na I D_1 $v_\odot$ (km s^{-1})	Na I D_1 b (km s^{-1})	Na I D_1 log N (cm^{-2})	K I λ7699 $v_\odot$ (km s^{-1})	K I λ7699 b (km s^{-1})	K I λ7699 log N (cm^{-2})
1	2	3	4	5	6	7	8	9	10	11
ϕ^1 Ori	S/N = 68; $W_\lambda = 155.8 \pm 0.5$ mÅ				S/N = 52; $W_\lambda = 215.6 \pm 0.9$ mÅ					
1	-9.26 ± 0.29	3.01 ± 0.44	10.50 ± 0.05	<0.27						
2	-1.74 ± 0.53	2.04 ± 0.50	10.60 ± 0.21	<0.18						
3a	3.07 ± 0.08	1.61 ± 0.19	11.11 ± 0.13	0.16	5.07 ± 0.45	4.40 ± 0.72	10.99 ± 0.06			
3b	4.67 ± 0.32	3.84 ± 0.22	11.69 ± 0.05							
4a	14.60 ± 0.09	3.63 ± 0.15	11.65 ± 0.02	0.50	11.83 ± 0.50	0.82 ± 0.66	10.34 ± 0.32			
4b					15.27 ± 0.54	1.81 ± 0.76	11.30 ± 0.19			
5	19.13 ± 0.24	1.65 ± 0.29	11.04 ± 0.14	1.62	18.03 ± 0.26	1.21 ± 0.56	11.25 ± 0.24			
6	21.35 ± 0.23	1.07 ± 0.33	10.91 ± 0.39	1.91	19.81 ± 0.07	0.64 ± 0.08	11.19 ± 0.10			
7a	23.31 ± 0.09	0.98 ± 0.11	11.52 ± 0.12	7.19	24.23 ± 0.09	1.61 ± 0.05	12.91 ± 0.05			
7b	24.96 ± 0.12	1.20 ± 0.12	11.67 ± 0.11		26.71 ± 0.24	0.88 ± 0.50	11.70 ± 0.59			
7c	25.53 ± 1.21	3.36 ± 0.64	11.66 ± 0.22		28.32 ± 1.64	1.64 ± 0.87	11.60 ± 0.62			
8	28.28 ± 0.03	0.40 ± 0.06	10.39 ± 0.06	14.79	28.43 ± 0.02	0.41 ± 0.05	11.56 ± 0.11			
β Ori	S/N = 139; $W_\lambda = 17.7 \pm 0.3$ mÅ				S/N = 192; $W_\lambda = 37.2 \pm 0.2$ mÅ			S/N = 78; $W_\lambda < 1$ mÅ		
1	-31.58 ± 0.06	0.71 ± 0.07	10.10 ± 0.05	<0.09						
2	-29.63 ± 0.25	1.14 ± 0.39	9.76 ± 0.12	<0.25						
3	-15.62 ± 0.04	1.81 ± 0.06	10.62 ± 0.01	0.30	-16.15 ± 0.29	3.83 ± 0.45	10.10 ± 0.04			
4				>3.47	-4.00 ± 6.29	3.83 ± 3.74	10.08 ± 0.98			
5	-0.68 ± 0.04	1.84 ± 0.06	10.68 ± 0.01	1.23	-0.70 ± 0.14	2.37 ± 0.41	10.77 ± 0.21			
6				>7.41	3.49 ± 0.29	1.99 ± 0.56	10.27 ± 0.17			
7a†	8.90 ± 0.10	1.31 ± 0.08	10.77 ± 0.04	0.66	8.50 ± 0.14	3.04 ± 0.38	10.71 ± 0.05			
7b	10.87 ± 0.24	1.18 ± 0.21	10.29 ± 0.13							
8				>13.18	16.42 ± 0.04	0.58 ± 0.05	10.25 ± 0.07			
9				>16.98	16.71 ± 2.46	3.33 ± 1.69	10.74 ± 0.46			
10	17.93 ± 0.06	0.87 ± 0.08	10.05 ± 0.03	7.08	18.40 ± 0.11	1.33 ± 0.23	10.90 ± 0.22			
11				>22.39	18.85 ± 0.01	0.22 ± 0.02	10.27 ± 0.03			
12				>8.51	20.90 ± 0.07	0.61 ± 0.16	10.07 ± 0.33			
13	22.68 ± 0.08	0.54 ± 0.11	9.82 ± 0.09	2.88	22.41 ± 0.11	0.82 ± 0.15	10.28 ± 0.14			
14	24.07 ± 0.11	0.74 ± 0.17	9.89 ± 0.08	5.01	24.10 ± 0.07	0.98 ± 0.08	10.59 ± 0.04			
15	29.12 ± 0.10	1.30 ± 0.15	10.03 ± 0.04	<0.14						
κ Ori					S/N = 145; $W_\lambda = 121.1 \pm 0.3$ mÅ			S/N = 85; $W_\lambda = 5.1 \pm 0.2$ mÅ		
1					-4.83 ± 0.73	2.44 ± 0.57	10.49 ± 0.17			
2					-0.81 ± 0.18	2.21 ± 0.43	10.89 ± 0.12			
3					3.33 ± 0.15	2.46 ± 0.13	11.15 ± 0.03			
4†					14.95 ± 0.04	0.50 ± 0.04	10.27 ± 0.02			
5					16.79 ± 0.03	0.44 ± 0.03	10.77 ± 0.04			
6					17.76 ± 0.01	0.45 ± 0.02	11.34 ± 0.02	17.37 ± 0.05	0.17 ± 0.14	9.57 ± 0.07
7					18.86 ± 0.01	0.43 ± 0.02	11.50 ± 0.02	18.43 ± 0.12	0.03 ± 1.08	9.28 ± 0.89
8					20.25 ± 0.10	0.70 ± 0.04	11.87 ± 0.12	19.78 ± 0.64	0.62 ± 0.37	10.17 ± 0.62
9					21.05 ± 0.02	0.37 ± 0.05	11.38 ± 0.20	20.59 ± 0.92	0.54 ± 0.71	9.85 ± 1.27
10					21.32 ± 0.70	0.78 ± 0.46	11.34 ± 0.58			
11					23.45 ± 0.06	1.04 ± 0.06	11.04 ± 0.02			

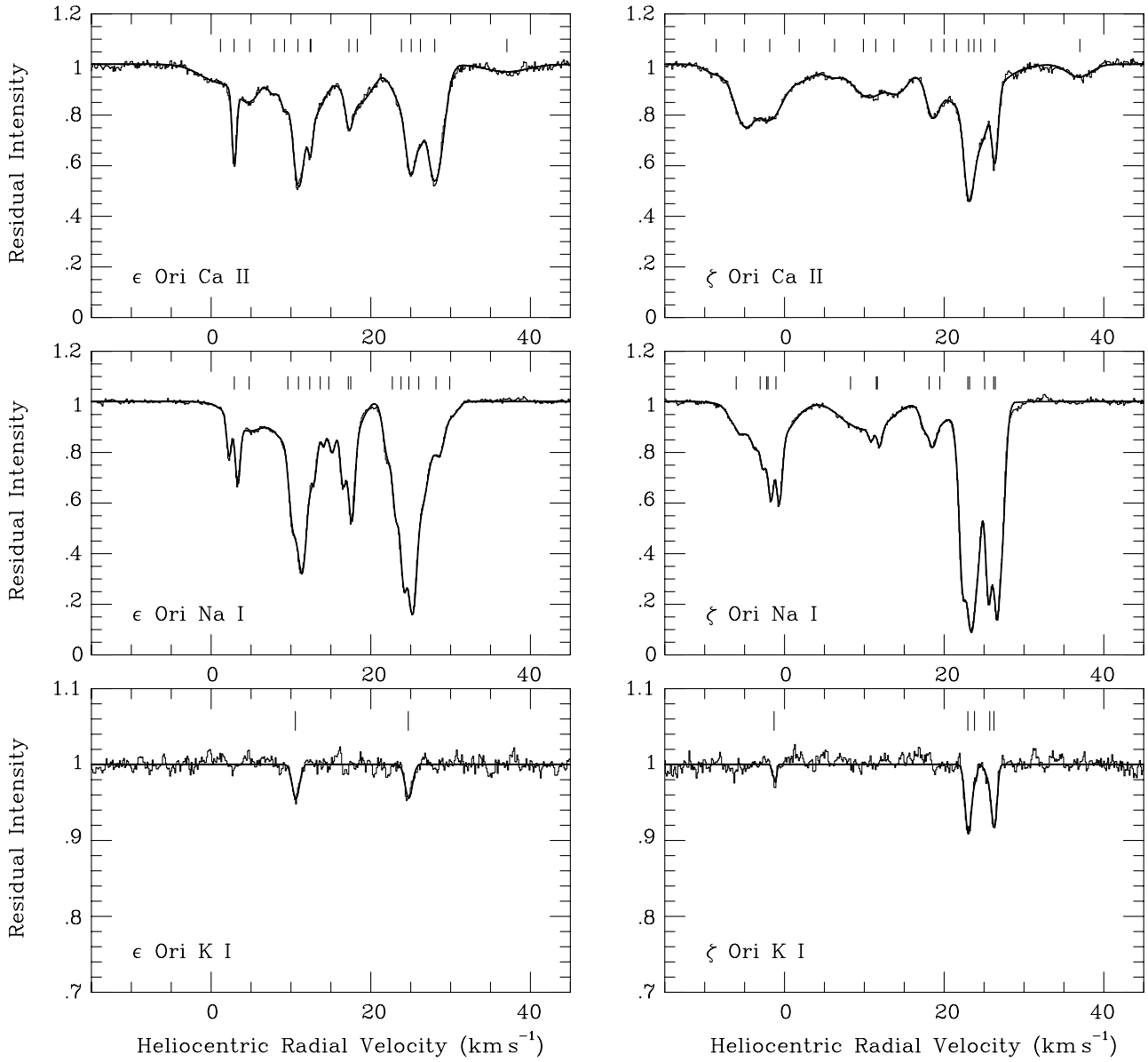

Figure 1. Theoretical line-profile fits (thick solid line) are shown plotted over the observed interstellar spectra (thin solid line) for 12 Orion stars. In some cases, the vertical scale has been expanded to display weak absorption more clearly. Tick marks are used to indicate the velocities of the individual model components, as listed in Table 3. In the case of both Na I and K I absorption components, the tick marks represent the weighted mean velocities for the two hyperfine components. Residual telluric contamination is indicated by the $\oplus$ symbol.

implying the existence of small-scale structure in this direction on scales of ≤ 0.07 pc (the projected separation of the two stars).

4.2 ζ Orionis

The Ca II observations of ζ Ori presented here and by W96 were obtained with the UHRF in 1994 January and February, respectively, and agree extremely well, demonstrating consistent data reductions (and zero-level determinations). However, comparison of the Na I spectrum of ζ Ori presented in this study with the absorption model published by W94 (generated from an observation made some six years earlier with $R \approx 6 \times 10^5$) reveals the presence of apparent variations at a velocity of $-1\,\mathrm{km\,s^{-1}}$. Further minor variations are also present between the velocities of $+5$ and $+15\,\mathrm{km\,s^{-1}}$, but can however be easily ascribed to small differences in continuum normalization. This comparison is shown graphically in Fig. 2(a). A further comparison can be made between the earlier, lower-resolution observation presented by H69. While this reveals a possible variation at $+19\,\mathrm{km\,s^{-1}}$, its authenticity is much less certain. Fig. 2(b) shows a comparison between our data and a spectrum digitized from the plot presented by H69.

Although W94 are able to model the -10 to $+4\,\mathrm{km\,s^{-1}}$ region of the ζ Ori Na I spectrum using only two components, there is evidence for highly blended substructure, which has been resolved (at least partially) by our UHRF observations. A re-evaluation of our Na I absorption model shows that, by reducing the column density of component 2e† (located at $-1.07\,\mathrm{km\,s^{-1}}$)

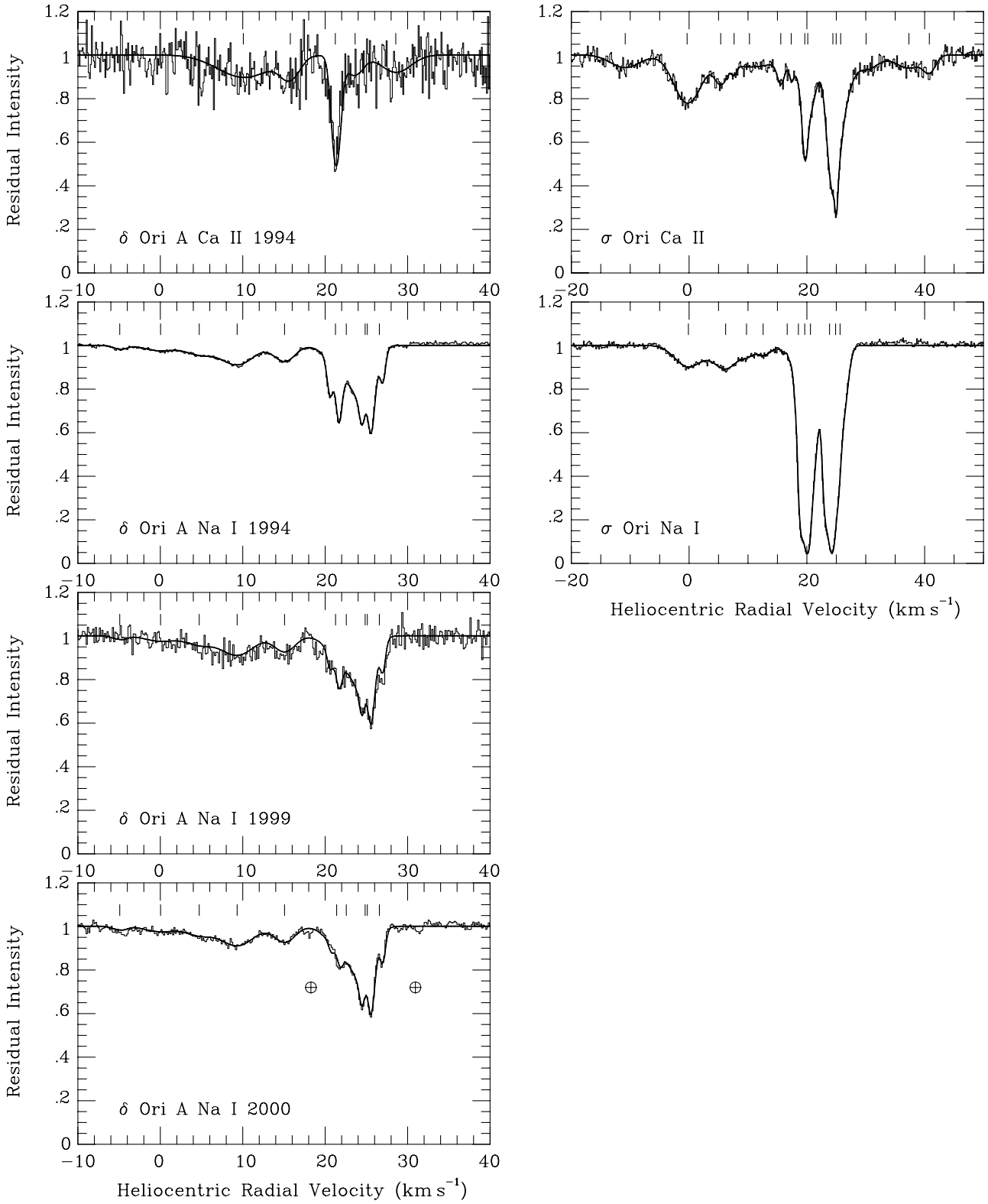

Figure 1 – *continued*

from $\log N = 10.98 \pm 0.02$ to $\log N = 10.45 \pm 0.05$ (with all other parameters held constant), it becomes possible to achieve good agreement with the absorption observed by W94. This represents a factor of 3.4 ± 0.6 increase in the Na^0 column density over a period of $\approx$6 yr. If the spectrum we have digitized from H69 is assumed to be an accurate representation of the Na I absorption at that time, a similar analysis may be conducted for component 2e† for the period 1966–1988. This yields a column density of

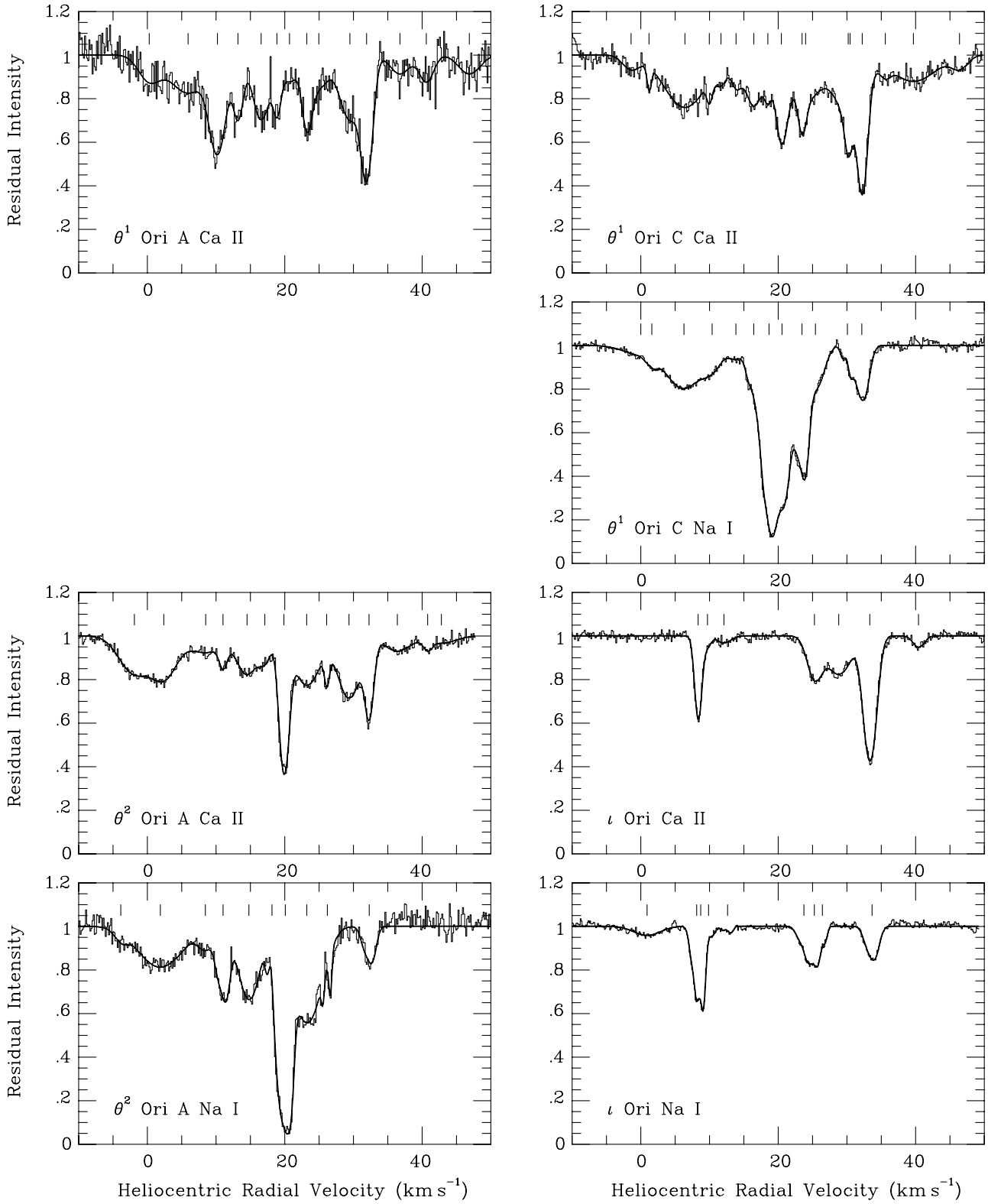

Figure 1 – *continued*

$\log N = 11.25 \pm 0.04$ for component 2e†. Similarly, for component 6† (located at $+18.11\,\mathrm{km\,s^{-1}}$), by decreasing the column density from $\log N = 10.66 \pm 0.05$ to $\log N = 10.42 \pm 0.05$ (all other parameters held constant), it becomes possible to achieve good agreement with the absorption observed by W94. By increasing the column density of component 6† to $\log N = 10.82 \pm 0.09$, optimum agreement is achieved with the observation of H69. Fig. 2(c) demonstrates both of these simulations graphically.

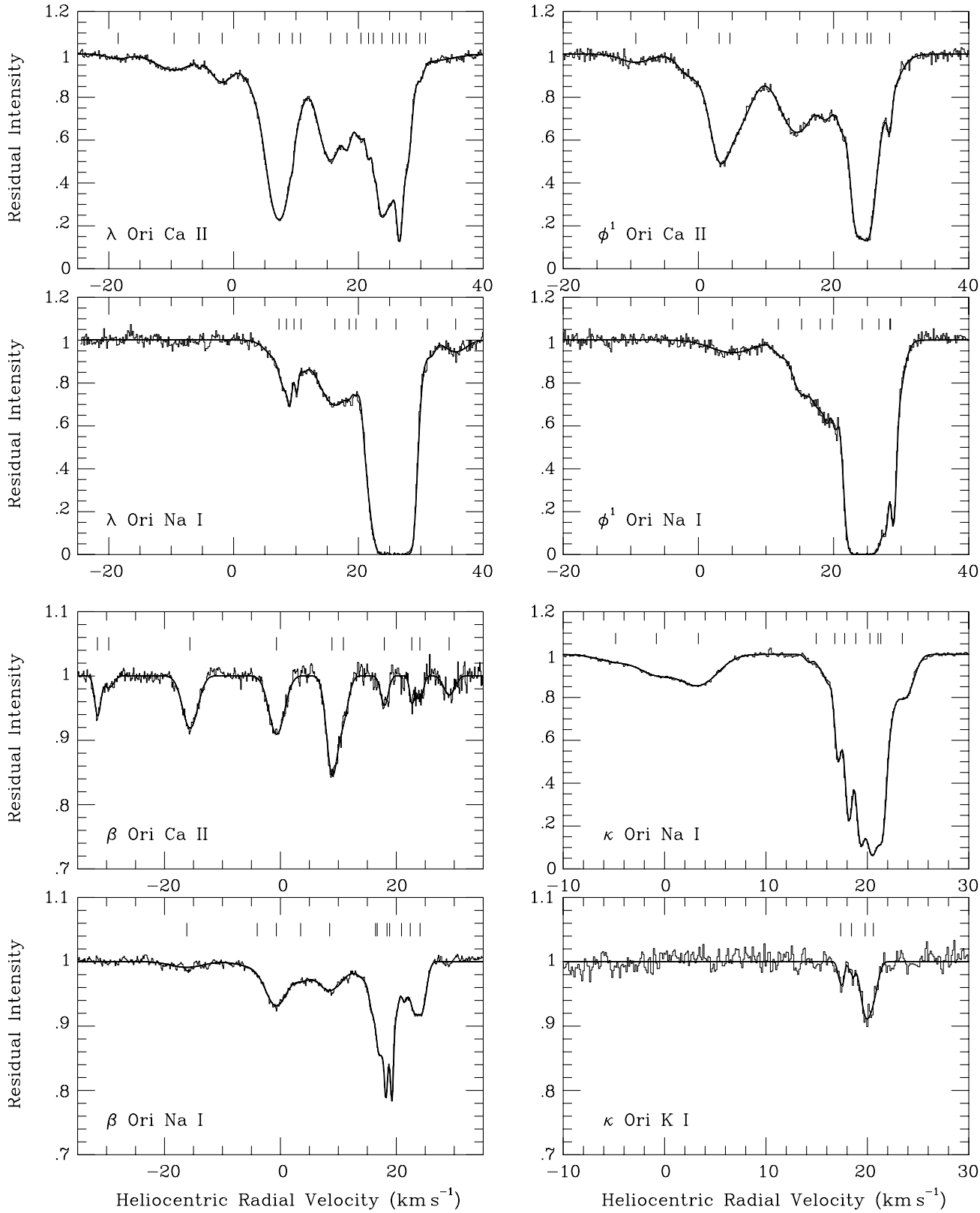

Figure 1 – *continued*

While only the increase in column density of component 2e† between approximately 1988 and 1994 is considered to be reliable, our measurements suggest a factor of 6.3 ± 1.4 reduction in the Na^0 column density of the $-1.07\,km\,s^{-1}$ cloud between 1966 and the late 1980s, subsequently followed by a factor of 3.4 ± 0.6 increase in the Na^0 column density by 1994. In the case of the $+18.11\,km\,s^{-1}$ cloud, a factor of 2.5 ± 0.9 reduction in its column density was observed between 1966

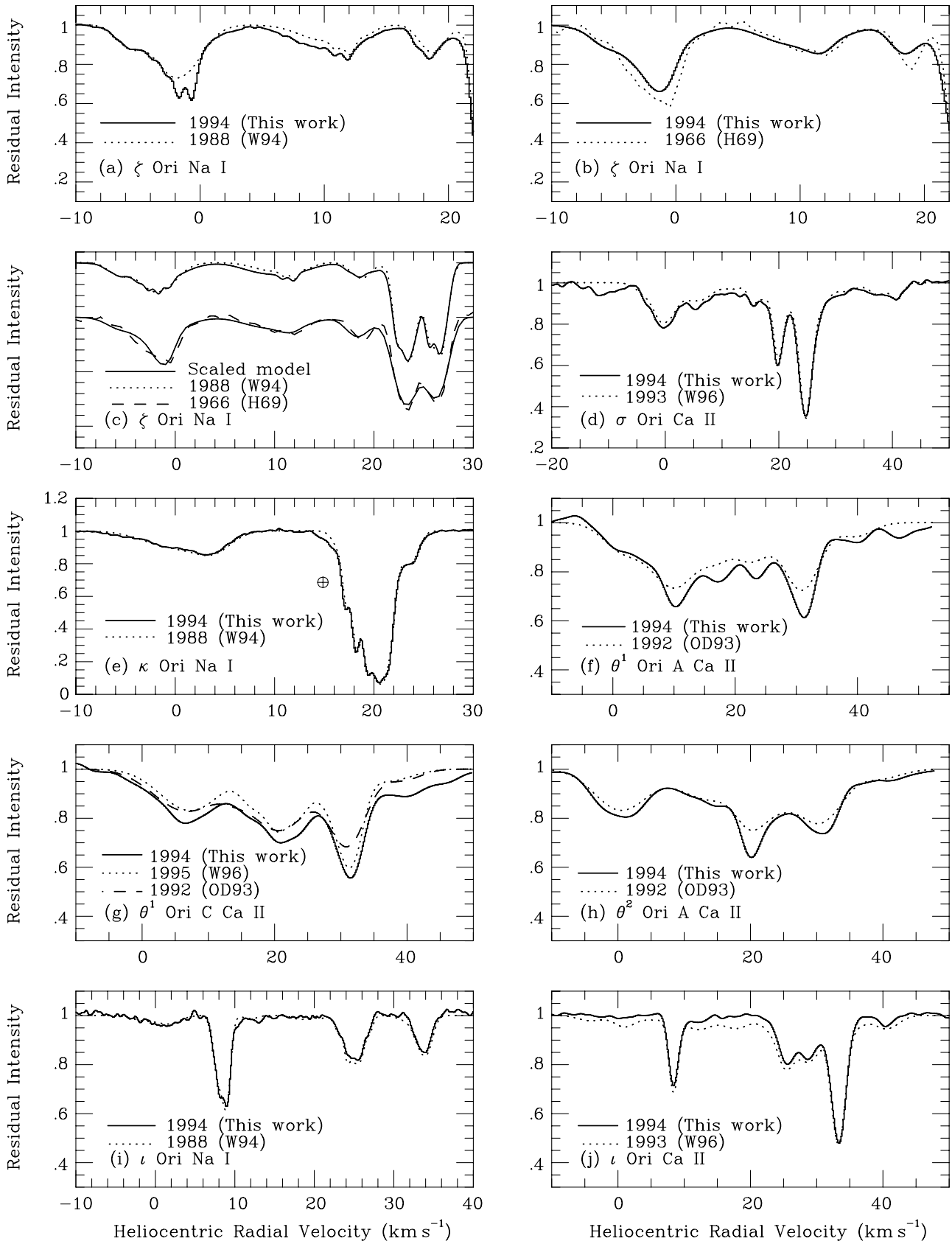

Figure 2. Comparison of our UHRF spectra with those presented in previous studies. Where spectra have been overplotted, a common *effective* resolving power has been used, equal to that of the lowest-resolution spectrum (detailed in Section 4). Part (c) shows a version of our Na I model for ζ Ori in which the column densities of components 2e† and 6† have been scaled to achieve optimum agreement with the data of H69 and W94. Residual telluric contamination is indicated by the $\oplus$ symbol.

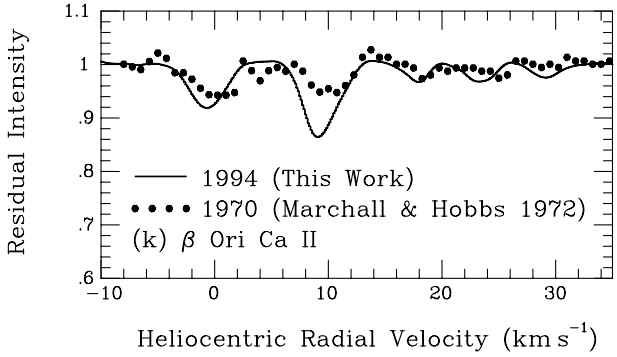

Figure 2 – *continued*

Table 4. Signal-to-noise ratios achieved for observations of CH λ4300 and CH^+ λ4232, along with 2σ upper limits to the equivalent widths (W_λ) and column densities (N), assuming representative b values of 1.7 and 2.4 km s^{-1} for the CH and CH^+ lines respectively (based on previous UHRF observations; e.g. Crawford 1995).

Star	Molecule	S/N	W_λ (mÅ)	log N (cm^{-2})
θ^1 Ori C	CH	52	≤0.6	≤11.8
θ^1 Ori C	CH^+	41	≤0.9	≤12.0
θ^2 Ori A	CH	62	≤0.5	≤11.8
θ^2 Ori A	CH^+	41	≤0.9	≤12.0
λ Ori	CH^+	65	≤0.6	≤11.8
ϕ^1 Ori	CH^+	37	≤1.0	≤12.0

and the late 1980s, followed by a factor of 1.7 ± 0.4 increase by 1994.

Temporal variations over such a small time period imply that the absorption occurs in a spatially small parcel of gas (at least in the transverse direction). Jenkins & Peimbert (1997) and Jenkins et al. (2000) have suggested that molecular hydrogen observed towards ζ Ori at a velocity corresponding to that of component 2e† may be produced in the compressed region behind a bow shock present in this direction (discussed further in Section 7.3).

Although the presence of a shock may account for the observed temporal variability, a small tangential displacement of the cloud, or the line of sight, as a result of the proper motion of ζ Ori, causing a shift in the line of sight probed, provides an equally likely explanation (as invoked for δ Ori in Paper I). In the case of ζ Ori (which has a proper motion of 4.73 mas yr^{-1}; ESA 1997), the increase in column density of component 2e† between approximately 1988 and 1994 highlights the presence of structure in the ISM down to scales of ≈7 au. Indeed, Lauroesch, Meyer & Blades (2000) have also observed temporal variability in Na I towards HD 32039/40 over scales of ≈ 15–21 au (inferred from the proper motion of the system). However, the analysis of Lauroesch et al. (2000) assumes the cloud to be stationary. By assuming a plausible upper limit of 50 km s^{-1} for the tangential velocity of our cloud, the linear distance traced across the cloud may be as high as ≈70 au, highlighting the importance of possible cloud motion.

The narrow linewidths of these temporally variable components seem typical of small-scale structure observed elsewhere (Papers I and II and references therein).

4.3 σ Orionis

A comparison of Ca II K observations towards σ Ori (shown in Fig. 2d) appears to reveal the appearance of an absorption component, in our 1994 spectrum, at a velocity of −10.85 km s^{-1}. An examination of the original 1993 spectrum published by W96 illustrates the presence of a very weak feature at this velocity, indicating that absorption was present, but unmodelled by W96. The differences in the absorption models therefore do not represent true variability in the absorption-line profiles.

4.4 κ Orionis

Exceptional agreement is seen between the Na I observations of κ Ori (shown in Fig. 2e) presented by W94 and this study, apart from the presence of a weak additional component in our spectrum at a velocity of +14.95 km s^{-1}. However, the +8 to +16 km s^{-1} range in this spectrum does suffer from some telluric absorption. This component is most probably not variable but instead the result of some residual contamination.

4.5 θ^1 Orionis A and C and θ^2 Orionis A

Less agreement is seen between the different Ca II spectra of θ^1 Ori A and C and θ^2 Ori A (Figs 2f–h). Comparison of the available spectra for these stars shows the overall forms of the absorption profiles to agree reasonably well, while the cores of the absorption lines are consistently deeper in the UHRF spectra, despite convolution with an appropriate Gaussian profile. This is echoed by equivalent-width measurements, which show the strength of absorption present towards both θ^1 Ori A and C to be slightly larger in the UHRF data as compared with OD93. The total Ca II K equivalent widths reported by OD93 for θ^1 Ori A and C are 105.5 ± 2 and 101 ± 2 mÅ respectively, compared to 119.2 ± 1.9 and 120.7 ± 1.2 mÅ found here. Hobbs (1978b) found the equivalent width of Ca II K absorption towards θ^1 Ori C to be 120 ± 5 mÅ, in good agreement with our results, while W96 quote 94.4 ± 0.7 mÅ and highlight the disagreement in equivalent-width measurements for this star. While this effect may be the result of inaccurate zero- and/or continuum-level determinations in our own or previous studies, the saturated Na I D_1 absorption present in UHRF spectra of λ and ϕ^1 Ori (discussed in Section 2) suggests the uncertainty in the zero level of the UHRF data to be small. We do note the lack of a well-determined red-wing continuum in the Ca II spectra of θ^1 Ori A and C and θ^2 Ori A, which does lead to the possibility of errors in the continuum normalization; however, this should, if anything, act to *reduce* both the measured equivalent widths and the absorption core depths.

The Na I D_2 spectrum of θ^1 Ori C published by Hobbs (1978b), and used by OD93 in their analysis of M42, contains an absorption feature at a velocity of +37.7 km s^{-1}. This component is associated with Ca II absorption seen by OD93 at +39.5 km s^{-1}. However, this Na I D_2 feature is in proximity to a telluric line (Hobbs 1978a) and is likely to be the result of telluric contamination. Furthermore, the very weak Na I D_2 components observed towards θ^1 Ori C and θ^2 Ori A at ≈ −16 km s^{-1} by Hobbs (1978b), and unexplained by OD93, are not observed here. The original θ^1 Ori C and θ^2 Ori A Na I D_2 spectra highlight the presence of possible telluric absorption at this velocity (also identified in the telluric template presented by Hobbs 1978a), which we confirm as having a telluric origin, using separate atmospheric templates of the Na I D_2 region obtained by us.

Since much of the absorption present towards these three stars is considered to arise in clouds located in proximity to M42 (see Section 7.1.3), a certain amount of temporal variability might be expected from such an energetic environment. However, attributing the observed differences in the line profiles to intrinsic variability in the absorption is difficult because of a lack of previous very high-resolution data. We conclude that there is no secure evidence as yet for significant variability in these sightlines.

4.6 ι Orionis

Although W94 identify several additional weak components in their Na I spectrum of ι Ori, excellent agreement is still seen with our observations (see Fig. 2i). With regards to the Ca II region, however, additional weak components identified by W96 *do* produce a noticeable difference (see Fig. 2j); however, we feel that these differences are unlikely to be the result of temporal variability and are easily attributable to differences in continuum normalization.

4.7 β Orionis

Although a comparison of our Ca II spectrum with that presented by Marschall & Hobbs (1972) can be made in order to search for temporal variability (Fig. 2k), the intrinsically weak nature of these lines, and the presence of a strong stellar line, both create problems with this procedure. The strength of the absorption present around $0\,\mathrm{km\,s^{-1}}$ appears similar in both studies, but that near $+9\,\mathrm{km\,s^{-1}}$ (our cloud 7a) appears somewhat weaker in the Marschall & Hobbs data, indicating possible temporal variability in this component. As discussed in Section 7.4, variability, coupled with ongoing mass loss, suggests a circumstellar origin. Further absorption, below a velocity of $-10\,\mathrm{km\,s^{-1}}$, is also thought to arise within the circumstellar environment of β Ori (Section 7.4), but an insufficient blueward range in the Marschall & Hobbs (1972) spectrum does not permit a comparison for these components.

5 CLOUD KINETIC TEMPERATURES AND TURBULENT VELOCITIES

Interstellar line broadening is dominantly the result of two effects, namely Doppler broadening due to (a) the kinetic temperature of the absorbers, T_k, and (b) the line-of-sight rms turbulent velocity within the cloud, v_t. If the velocity spectrum of the turbulence is Gaussian, then the b value resulting from these two broadening mechanisms is described by

$$b = \sqrt{\frac{2kT_\mathrm{k}}{m} + 2v_\mathrm{t}^2}, \qquad (1)$$

where the observed line FWHM $= 1.665b$, k is Boltzmann's constant and m is the mass of the relevant atom/ion (see Cowie & Songaila 1986). Thus by observing two species that are considered to exist co-spatially, and which have an adequate mass differential, e.g. Na and K, it becomes possible to solve equation (1) simultaneously for both T_k and v_t (see Dunkin & Crawford 1999). Where the best-fitting b values of corresponding Na I and K I components provide a solution to equation (1), 'exact solutions' are said to be obtained (see columns 7–10 of Table 5). Furthermore, 1σ error limits quoted in Table 3 have also been adopted for each b value, providing a range of allowed solutions to equation (1) (see columns 11–14 of Table 5). Since these calculations depend

Table 5. Values of kinetic temperature (T_k), turbulent velocity (v_t), three-dimensional turbulent velocity ($\equiv\sqrt{3}v_\mathrm{t}$) and isothermal sound speed (C_s; relating to atomic H with 10 per cent He by number) for clouds simultaneously observed in two co-extensive species. Columns 1, 2 and 3 show the sightline studied and its total column densities of H I and H_2. Column 4 displays the species used in the analysis, while columns 5 and 6 display the component number and the heliocentric radial velocity (taken from the Na I counterpart, as listed in Table 3). Columns 7–10 display exact solutions, where available, while columns 11–14 display all values allowed within the 1σ error limits quoted in Table 3. In the cases where no solutions within the 1σ error bounds are available, 2σ error limits are invoked and the results are discussed in the text.

Star	$\log[N]_\mathrm{tot}$ [H]	$\log[N]_\mathrm{tot}$ [H_2]	Method	Cloud	$v_\odot$ ($\mathrm{km\,s^{-1}}$)	T_k (K)	v_t ($\mathrm{km\,s^{-1}}$)	$\sqrt{3}v_\mathrm{t}$ ($\mathrm{km\,s^{-1}}$)	C_s ($\mathrm{km\,s^{-1}}$)	ΔT_k (K)	Δv_t ($\mathrm{km\,s^{-1}}$)	$\Delta\sqrt{3}v_\mathrm{t}$ ($\mathrm{km\,s^{-1}}$)	ΔC_s ($\mathrm{km\,s^{-1}}$)
1	2	3	4	5	6	7	8	9	10	11	12	13	14
ϵ Ori	20.45	16.57	Na I/Ca II	2	2.90	86	0.17	0.30	0.75	22–148	0.11–0.22	0.18–0.39	0.38–0.98
			Na I/K I	5	10.94	355	0.26	0.46	1.52	0–584	0.00–0.43	0.00–0.75	0.00–1.96
			Na I/K I	11	24.77	77	0.37	0.65	0.71	0–404	0.18–0.42	0.32–0.73	0.00–1.63
ζ Ori	20.41	15.73	Na I/K I	2e†	−1.07	–	–	–	–	0–293	0.00–0.33	0.00–0.56	0.00–1.38
			Na I/K I	8a	22.97	–	–	–	–	–	–	–	–
			Na I/K I	8b	23.19	–	–	–	–	–	–	–	–
			Na I/K I	11a	26.20	–	–	–	–	0–101	0.00–0.19	0.00–0.33	0.00–0.81
			Na I/K I	11b	26.41	–	–	–	–	508–841	0.00–0.30	0.00–0.52	1.82–2.35
κ Ori	20.52	15.68	Na I/K I	6	17.76	–	–	–	–	–	–	–	–
			Na I/K I	7	18.86	–	–	–	–	0–280	0.00–0.32	0.00–0.55	0.00–1.35
			Na I/K I	8	20.25	356	0.34	0.59	1.53	0–757	0.00–0.52	0.00–0.91	0.00–2.23
			Na I/K I	9	21.05	–	–	–	–	0–244	0.00–0.30	0.00–0.51	0.00–1.26

critically on the component structures obtained from our models, this type of analysis is best suited to isolated velocity components, where confusion with nearby blended absorption is at a minimum. Furthermore, for the intrinsically weak K I line to be detectable, the Na I D_1 line must be strong, but not saturated. In order for these results to be meaningful, the intrinsic widths of the lines must be determined, something best suited to very high-resolution, high signal-to-noise ratio data.

The derived value of T_k can subsequently be used to determine the isothermal sound speed, C_s, in a cloud, using the relation

$$C_s = \sqrt{\frac{kT_k}{\mu}}, \tag{2}$$

where μ is the mean mass per particle, here assumed to be $1.27m_H$, i.e. an atomic H gas containing 10 per cent He by number (e.g. Spitzer 1978). Positive detections of molecular hydrogen have been made towards ϵ, ζ and κ Ori at velocities corresponding to each K I component (see fig. 3 of Jenkins et al. 2000; fig. 7 of Jenkins & Peimbert 1997; and table 1 of Spitzer & Morton 1976). The presence of molecular hydrogen in these clouds will of course increase the mean mass per particle, therefore reducing the prevailing isothermal sound speed; however, the column densities of molecular hydrogen are seen to be small with respect to those of hydrogen (total H I and H_2 column densities are shown in Table 5, taken from Savage et al. 1977). In reality H_2 is likely to be preferentially found in the same (colder/denser) regions where the Na I and K I absorption is thought to arise, but the fraction of hydrogen in the molecular form is still expected to be small. Even if 50 per cent of the H atoms in these regions were to be in the molecular form, μ will be $1.65m_H$, only resulting in an $\approx$14 per cent decrease in C_s.

Observations of both Na I and K I have been made for the sightlines towards β, ϵ, ζ and κ Orionis, which we discuss below.

5.1 β Orionis

Absorption from K I has not been positively identified towards β Ori. This is consistent with the relatively weak strength of Na I towards this star. Although our sample of Na I, K I pairs is far too small for a meaningful statistical analysis, a comparison of Na^0 and K^0 column densities shows a typical ratio $Na^0/K^0 \approx 60$, leading to an expected K^0 column density towards β Ori of only $\log N \approx 9.00$ from the strongest Na I component, which is below our detection threshold.

5.2 ϵ Orionis

Observations of K I towards ϵ Ori reveal the presence of two main components. The higher-velocity component exhibits slight asymmetry, although it can be accurately modelled with a single absorbing cloud. Exact solutions are achievable for both clouds and show both v_t and $\sqrt{3}v_t$ to be subsonic. Only in the extreme case where the majority of H is present in the molecular form does the sound speed of ϵ Ori's $+24.77\,km\,s^{-1}$ component permit supersonic, three-dimensional turbulent motions. Over the full 1σ error range, supersonic turbulence is only permitted when T_k resides near its lower limit.

A very narrow Na I absorption component with one of the clearest examples of HFS is present at a velocity of $+2.90 \pm 0.01\,km\,s^{-1}$. Although too weak to be accurately modelled, a possible signature of K I absorption is present at a similar velocity ($\approx +2.7\,km\,s^{-1}$), with an equivalent width of $\leq$0.5 mÅ. Furthermore, a comparison of the Na I and Ca II spectra of ϵ Ori illustrates a narrow Ca II absorption component at a velocity of $+2.88 \pm 0.01\,km\,s^{-1}$. This system is a clear example of both Na I and Ca II absorption from a cool cloud occurring at (within the errors) the same velocity. By assuming the case of purely thermal ($v_t = 0$) or purely turbulent ($T_k = 0$) broadening, it is possible to place strict upper limits on both the T_k and v_t prevailing in the regions where the Na I and Ca II absorption is occurring, without having to assume that the species are co-spatial. In the case of Na^0, $T_k \leq 169\,K$ and $v_t \leq 0.25\,km\,s^{-1}$, while for Ca^+, $T_k \leq 231\,K$ and $v_t \leq 0.22\,km\,s^{-1}$.

It is generally observed that line broadening in Ca II is greater than that seen in Na I (interpreted to be due to Ca^+ preferentially occupying the warmer outer regions of a cloud; e.g. Barlow et al. 1995). However, in this case it is Na I that is seen to exhibit the largest broadening. The fact that the lighter Na atom is subjected to greater broadening may signify that the species exist co-spatially. This being the case, it is possible to solve equation (1) in the same way as has been done for Na I and K I (see first entry of Table 5). Both the line-of-sight and three-dimensional turbulent velocities are well below the corresponding sound speeds for either a purely atomic or a purely molecular gas, indicating the turbulence to be subsonic in all cases. We find that three-dimensional supersonic turbulent motions are only permitted in an atomic gas when T_k is *at* its lower limit. It is interesting to note that, while this cloud is cold, it has a Na^0/Ca^+ ratio of 1.78, illustrating that not all the Ca has been depleted. Since Ca is rapidly depleted on to grain surfaces (Barlow et al. 1995), the recent removal of Ca atoms from grains would be implied, consistent with Na and Ca being co-extensive.

5.3 ζ Orionis

Between velocities of +20 and $+30\,km\,s^{-1}$, the IS Na I spectrum of ζ Ori is dominated by two features. Modelling of these two features requires five components for a satisfactory fit. Examination of this star's K I IS spectrum echoes the presence of the two major Na I features, but further investigation reveals the components to be asymmetric, such that four of the five Na I components have corresponding K I components. The highly blended nature of this region leads, in general, to larger errors for the weak K I components. An additional weak K I component is also present at $-1.31\,km\,s^{-1}$, corresponding to the temporally variable Na I component at $-1.07\,km\,s^{-1}$ (see Section 4.2).

None of the velocity components permit exact solutions for T_k and v_t, while clouds 8(a) and 8(b) do not allow any physical solutions within their respective 1σ error ranges. In this case, 2σ error ranges can be applied, resulting in an allowed range for T_k and v_t for both clouds. Within the 2σ error range of cloud 8(a), $T_k < 92\,K$ while $0.18 < v_t < 0.25$. In the case of cloud 8(b), $T_k < 1023\,K$ and $v_t < 0.61$. In the case of cloud 11(b), the line-of-sight and three-dimensional turbulence is subsonic, even in a molecular gas. For the remaining clouds, supersonic turbulence is only allowed when T_k is near its lower limit.

5.4 κ Orionis

Observations of K I towards κ Ori reveal the presence of two absorption features, near +18 and $+20\,km\,s^{-1}$. Although both regions can be accurately fitted with a single component, the $+20\,km\,s^{-1}$ feature coincides with three strong Na I components

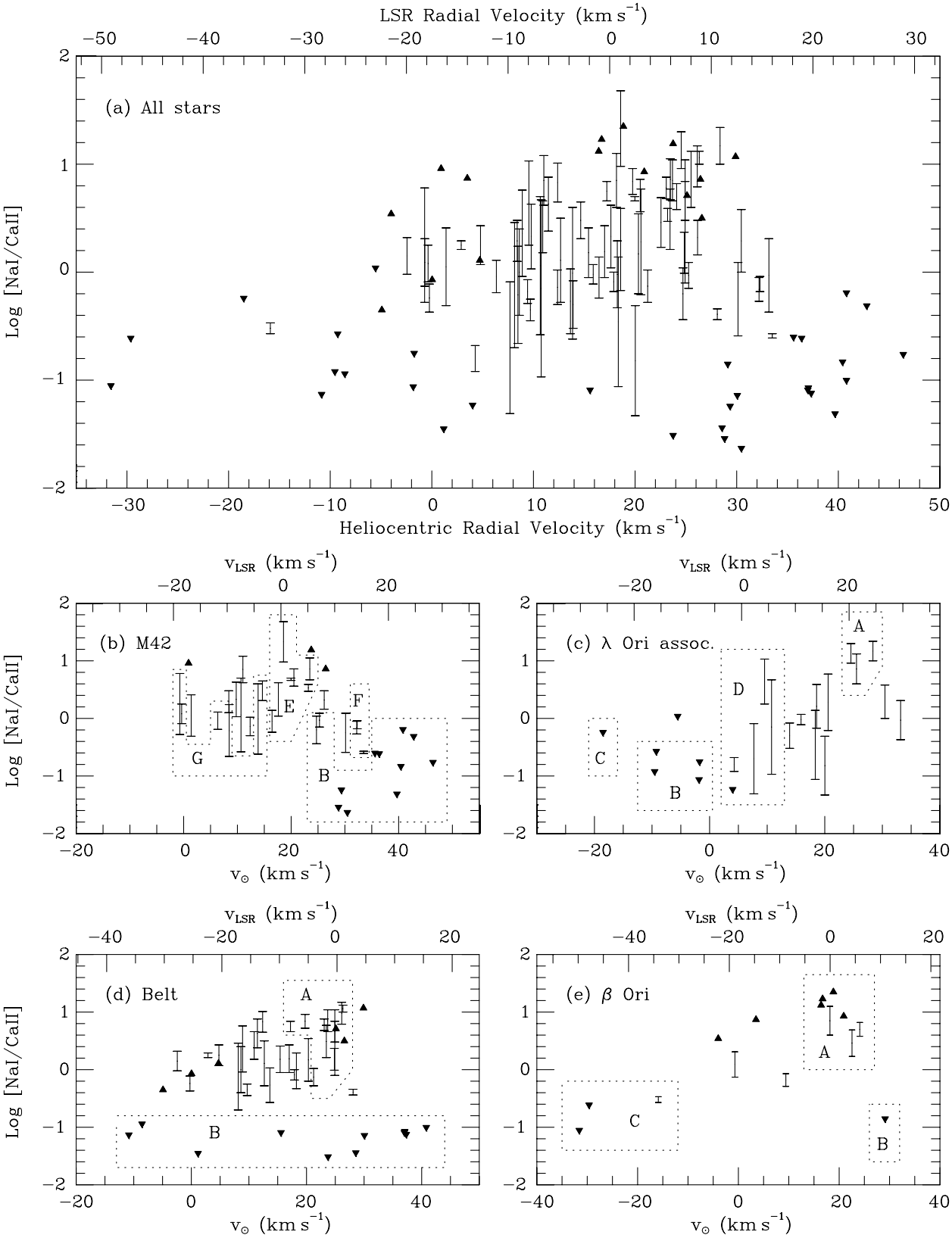

Figure 3. Na^0 to Ca^+ column density ratios plotted as a function of radial velocity (upward- and downward-pointing triangles represent lower and upper limits, respectively). Part (a) shows all clouds identified towards the Orion stars, and parts (b)–(e) display clouds identified in selected sightlines, and illustrate the broad groupings discussed in Section 6. The groupings are complete in the most part; however, there are a small number of instances where it has not been possible to include points in their correct group.

and so has been modelled with three corresponding K I components.

Only cloud 8 permits exact solutions for T_k and v_t, while cloud 6 has no physical solutions within its 1σ error range. If 2σ errors are applied to cloud 6, we find $T_k < 332$ K and $v_t < 0.32$. Supersonic turbulence is again only permitted when T_k is near its lower limit.

A comparison of v_t and $\sqrt{3}v_t$ with C_s from the available exact solutions to equation (1) (Table 5, columns 7–10) demonstrates the turbulent motions to be subsonic in all cases. If a molecular gas is assumed, only ϵ Ori's cloud 11 permits supersonic three-dimensional turbulent motions, if 50 per cent or more of the H nuclei are in the form of H_2.

Similarly, where exact solutions are not available, a comparison of the range of turbulent velocities and sound speeds permitted within the adopted b value error ranges (shown in Table 5, columns 11–14) indicates that the turbulent motions are generally subsonic, unless T_k is near its lower limit. However, this is subject to a selection effect. In the two extreme cases where either T_k or v_t is zero, we find that the allowed b values of the two observed species range from being equal to differing by a factor equal to the square root of their mass ratio, respectively. Outside this range, no physical solutions are permitted. Since the errors associated with the b values of K I are in general much larger than those of their Na I counterparts (weaker components, lower S/N), solutions for T_k and v_t are available for each b value allowed within the 1σ error range of several Na I components [clouds 2e† and 11a towards ζ Ori and clouds 7, 8 (although an exact solution is available for this cloud) and 9 towards κ Ori]. This illustrates that the line broadening in *both* species should be determined to a level of accuracy such that solutions for T_k and v_t are not obtainable over the entire range of permitted b values of either of the species. If this is not achieved, the range of permitted values of T_k and v_t is not restricted any further than that which may be obtained from the observation of a single species.

Where solutions for T_k and v_t are available for each b value within the Na I error range, 95 and 92 per cent of these possible solutions describe subsonic turbulence in purely atomic and purely molecular gas, respectively. When considering the perhaps more realistic case of three-dimensional turbulence ($\equiv\sqrt{3}v_t$), these values fall to 87 and 79 per cent, again for a purely atomic and a purely molecular gas, respectively. This illustrates that, in these cases, the range of permitted values will inherently show turbulence to remain subsonic unless T_k resides near its lower limit.

6 Na^0/Ca^+ ABUNDANCE RATIOS

It has long been recognized that interstellar absorption components display a very wide range of Na^0/Ca^+ ratios. This is primarily due to variations in the gas-phase abundance of Ca, governed by a balance between preferential Ca adsorption on to grain surfaces in quiescent dense environments, and removal from grain surfaces by shocks and sputtering in energetic environments (e.g. Jura 1976; Barlow & Silk 1977; Barlow 1978; Phillips, Pettini & Gondhalekar 1984). Although interpretation is complicated by the fact that Ca^+ and Na^0 do not necessarily dominate in the same regions of an interstellar cloud (e.g. Barlow et al. 1995), in those cases where an origin in the same cloud can plausibly be assumed, the Na^0/Ca^+ ratio can yield information on the prevailing physical conditions (Crawford 1992).

Na^0/Ca^+ ratios have been calculated for each of the clouds identified in these data (column 5, Table 3). Where a single Na I component corresponds well to a single Ca II component, a Na^0/Ca^+ ratio is derived for the cloud. Where one or more Na I components correspond to one or more Ca II components, a mean Na^0/Ca^+ ratio is given for the system as a whole. Error limits on the ratio are found by calculating the range of Na^0/Ca^+ ratios allowed within the error bounds of the Na^0 and Ca^+ column densities. In the situation where a Na I or Ca II component has no corresponding Ca II or Na I component, lower and upper limits to the Na^0/Ca^+ ratio are given by calculating upper limits to associated absorption that may be present but undetected. Following Welsh et al. (1990) the 2σ upper limit to the equivalent width, W_λ, of an undetected line is found assuming

$$W_\lambda \leq \frac{2\Delta\lambda\sqrt{N_{\rm cont}}}{\rm S/N}, \tag{3}$$

where $\Delta\lambda$ is the width of one data pixel in Å, $N_{\rm cont}$ is the assumed width, in the continuum, of the undetected absorption line in pixels, and S/N is the continuum signal-to-noise ratio of the observation. Here, the FWHM of a Ca II line has been taken to be 1.3 times larger than that of a corresponding Na I line (found through the comparison of all Ca II, Na I pairs in Table 3) and the linewidth in the continuum is taken to be 2.5 times larger than the FWHM. The column density of the line is then found assuming

$$N \leq 1.13 \times 10^{20} \frac{W_\lambda}{f\lambda^2}, \tag{4}$$

where f is the oscillator strength of the transition (see Table 2) and W_λ and λ are both given in Å (Cowie & Songaila 1986). If an 'undetected' line is present in a blended region, the upper limit derived for N may be slightly underestimated.

Fig. 3(a) displays all calculated Na^0/Ca^+ ratios as a function of radial velocity (taken as a mean of the constituent components). Figs 3(b)–(e) show similar individual plots for the M42 region, the λ Ori association, the Belt stars and β Ori, respectively. Velocities with respect to the local standard of rest (LSR) and the Sun are marked at the top and bottom of each figure, respectively.

When considering Fig. 3(a) in terms of LSR radial velocities, a clear illustration of the fall-off of the Na^0/Ca^+ ratio with absolute radial velocity can be seen (Routly & Spitzer 1952). However, while Routly & Spitzer (1952) surmised that clouds with small Na^0/Ca^+ ratios are preferentially found at larger absolute velocities, further investigation of Fig. 3(a) shows such clouds to be distributed throughout the velocity range. The situation is therefore more likely to be that clouds with small Na^0/Ca^+ ratios possess a larger distribution of velocities. Furthermore, additional clouds characterized by low Na^0/Ca^+ ratios are likely to be present at low absolute velocities but simply masked by the much stronger absorption from the colder/denser clouds that generally occupy these velocities. A similar effect was noted by Crawford, Barlow & Blades (1989) in their study of the ISM towards the Sco OB1 association.

Anticipating the discussion in the next section, many of the points in Figs 3(b)–(e) have been collected together into broad groups of clouds possessing similar characteristics. These groups are labelled with letters, representing: A) cold diffuse/molecular clouds B) warm intercloud gas C) possible mass-loss material D) λ Ori shell material E) M42 neutral lid F) M42 foreground clouds G) H II region(s) foreground to M42.

An inspection of the average radial velocities of cold diffuse/partially molecular clouds with larger Na^0/Ca^+ ratios (group A) highlights a small systematic change in radial velocity. In the south, κ Ori exhibits its strongest Na I absorption around

$+20\,\mathrm{km\,s^{-1}}$, in the Belt region this becomes $+22$ to $+25\,\mathrm{km\,s^{-1}}$, while it is at $+25\,\mathrm{km\,s^{-1}}$ for the λ Ori association. From the H I observations of the Orion–Eridanus shell presented by Brown et al. (1995) we see that the line of sight to the southern Orion stars may indeed preferentially intersect lower-velocity gas (cf. their fig. 8). This is consistent with our 'group A' absorption largely arising in the neutral gas marking the boundary of the Orion–Eridanus shell. Indeed, a spherical shell at a distance of 450 pc, centred at $(l, b) = (195°, -35°)$, with a radius of 200 pc, expanding at a rate of $45\,\mathrm{km\,s^{-1}}$, will show a reduction in the line-of-sight expansion velocity of $\approx 7\,\mathrm{km\,s^{-1}}$ between the sightlines towards λ Ori (in the north) and κ Ori (in the south). The absence of strong absorption towards stars in the M42 region and δ and β Ori are likely to be due to inhomogeneities in the shell.

7 DISCUSSION

7.1 The M42 region

M42 appears as a blister on the surface of OMC-1 and is generally assumed to be at a distance of 450 pc (e.g. Goudis 1982). This makes it the closest bright H II region, and therefore the best spatially resolved object in its class. It is the ultraviolet (UV) radiation produced by the nearby Trapezium cluster (primarily θ^1 Ori C) that creates the nebula's principal ionization front, eroding into OMC-1, and in turn giving rise to the optical emission. Ionized material expands away from the ionization front, with progressively higher ionization stages being detected at higher velocities relative to the front (OD93). Originally postulated by Zuckerman (1973), the idea of a 'neutral lid' lying across the face of M42 was advanced by O'Dell & Wen (1992, cf. their fig. 7) using the 21-cm absorption-line observations by van der Werf & Goss (1989). This lid itself possesses secondary ionization fronts on both its near and far sides (OD93, cf. their fig. 3). On its far side, ionization again comes primarily from θ^1 Ori C; however, emission from this region is observed to be much weaker than that from the principal ionization front, placing the front seven times further from θ^1 Ori C than the principal ionization front formed against OMC-1 (Wen 1993). On its near side, the ionization source is ι Ori, 31 arcmin distant (corresponding to a linear distance of $\approx$4 pc at the distance of M42; see Table 1), located in the foreground to the neutral lid (OD93).

Previous studies of the M42 region, such as the comprehensive investigation by OD93, have been able to generate three-dimensional models of the emission and absorption regions (cf. fig. 3 of OD93) but have relied on observations made at significantly lower resolutions. The resolution employed by OD93 ($3.3\,\mathrm{km\,s^{-1}}$ FWHM) in their Ca II K observations of the Trapezium stars is unable to reveal the complex structure present in the UHRF data, and perhaps leads to an incomplete view of the absorbing medium in this direction. To supplement their data set, OD93 digitized Na I D_2 spectra of θ^1 Ori C and θ^2 Ori A from Hobbs (1978b) and included them in their analysis.

Here we discuss our ultra-high-resolution observations of Ca II K towards θ^1 Ori A, and both Ca II K and Na I D_1 towards θ^1 Ori C, θ^2 Ori A and ι Ori. The increased resolution employed by this study has shown many of the components analysed by OD93 in fact to be blends of multiple components. In a number of cases, components seen in the UHRF data are themselves thought to be blends of still narrower lines (discussed later).

In the case of the M42 region, a particular effort has been made to identify individual velocity systems. By comparing the absorption models constructed from line fitting, it has been possible to segregate the absorption into such systems, where absorption occurring in each system is thought to arise in an individual IS cloud sampled by more than one sightline. The absorption components comprising each system are shown in Fig. 4 with identifiers of the form M***x***, where 'M' denotes 'M42' (in order to reduce confusion with individual clouds), and ***x*** is a number that increases with the system's mean central velocity. Throughout the following discussion of M42, the reader is referred to Fig. 5, which illustrates the line-of-sight velocity structure for the main absorbing systems in the direction of M42.

For the purpose of discussion, the material giving rise to absorption in this direction will be segregated into three main sections: Section 7.1.1 will be devoted to the 'neutral lid' (represented by group E in Fig. 3); the 'foreground H II region and secondary ionization fronts' will be discussed in Section 7.1.2 (represented by group G in Fig. 3); and Section 7.1.3 will discuss the 'foreground material' (represented by group F in Fig. 3). The remaining components are subsequently discussed in Section 7.1.4.

7.1.1 Neutral lid

The existence of the neutral lid was originally postulated by Zuckerman (1973) and later developed by O'Dell & Wen (1992) using observations made by van der Werf & Goss (1989), who identified three H I 21-cm absorption components at $+16$, $+21$ and $+24\,\mathrm{km\,s^{-1}}$ (which they label C, B and A respectively). These components are expanding away from OMC-1, which itself has a radial velocity of $+27\,\mathrm{km\,s^{-1}}$ (Goudis 1982). Component A corresponds to the H I in the envelope of OMC-1, component C is present in a layer between the ionization front and the shock front that precedes it, and component B is probably located between A and C (van der Werf & Goss 1989). OD93 identify three absorption systems (none of which are detected towards all four of the Trapezium stars) at velocities of $+15$, $+20$ and $+23\,\mathrm{km\,s^{-1}}$, where ordering along the line of sight corresponds to that adopted by van der Werf & Goss (1989).

The observations obtained here clearly demonstrate the presence of several components towards each star, with discernible absorption in both Na I and Ca II occurring at velocities corresponding to the aforementioned H I 21-cm components. Here we detect four systems (numbered **M12**, **M13**, **M14** and **M15**), with velocities of approximately $+17$, $+19$, $+20$ and $+23\,\mathrm{km\,s^{-1}}$ respectively (see Fig. 4). The ordering we adopt along the line of sight reflects that deduced by van der Werf & Goss (1989). None of these absorption systems are observed towards ι Ori, which displays an altogether less complicated spectrum, consistent with ι Ori being foreground to the neutral lid. We infer that H I components A and B correspond to our systems **M13**, **M14** and **M15**, the average Na^0/Ca^+ ratios measured for these systems being 21.4, 5.0 and 5.3 respectively (see Section 6 and Table 3), consistent with the partial depletion of Ca on to dust grains. System **M12**, on the other hand, which we associate with H I component C [which van der Werf & Goss (1989) locate between the ionization and shock fronts], possesses a much lower Na^0/Ca^+ ratio of $\approx$1.5. Although a shock velocity of $\approx 5\,\mathrm{km\,s^{-1}}$ is insufficient to remove adsorbed Ca from grain surfaces (e.g. Barlow 1978), the low Na^0/Ca^+ ratio suggests there to be little depletion.

The neutral lid absorption detected towards the two Trapezium stars, θ^1 Ori A and C, appears well correlated between both stars in Ca II and between Na I and Ca II towards θ^1 Ori C. Comparison of this absorption with that seen towards the

2.5-arcmin distant (projecting to a linear distance of 0.3 pc) θ^2 Ori A, while revealing some similarity, also reveals clear differences. This is consistent with the view of the region depicted by Peimbert (1982, cf. fig. 1), where both θ^2 Ori A and the Trapezium stars possess a shroud of neutral material, but are however segregated. Thus, the neutral lid components observed in each direction would not be expected to be identical. System M**12** is observed towards each of the stars although it appears slightly narrower and weaker towards θ^2 Ori A. The $\approx+20\,\mathrm{km\,s^{-1}}$ cloud observed towards θ^2 Ori A (in both Na I and Ca II) is located between the velocities of systems M**13** and M**14** observed towards the Trapezium stars. We associated it with system M**14**, which possesses a similar Na^0/Ca^+ ratio. This leaves system M**13**, with its large Na^0/Ca^+ ratio, only present towards the Trapezium.

The Na I and Ca II components detected towards θ^2 Ori A at a velocity of $23.2\,\mathrm{km\,s^{-1}}$ possess both a velocity and Na^0/Ca^+ ratio compatible with their association with system M**15** as observed towards θ^1 Ori A and C; however, their broad nature is inconsistent with cool H I gas [van der Werf & Goss (1989) estimate the H I spin temperature of this gas to be only $\approx$25 K, with a factor of 2 uncertainty], and we therefore suggest them to be the result of a blend of closely spaced, unresolved components, each arising within the neutral lid.

7.1.2 Foreground H II region and secondary ionization fronts

As discussed earlier, the neutral lid is itself thought to possess secondary ionization fronts on both its near and far sides. On its far side, emission from [O III] and [S III] is detected at $\approx +12\,\mathrm{km\,s^{-1}}$, while on its near side emission from [O II] and [O III] has been detected at a velocity of $\approx +3\,\mathrm{km\,s^{-1}}$ (OD93). While OD93 were unable to detect Ca II absorption arising in the far-side secondary ionization front in their own spectra, they do associate a Na I component observed towards θ^2 Ori A (from the spectra of Hobbs 1978b) with this region. With regards to the near-side secondary ionization front, OD93 detect Ca II absorption towards θ^1 Ori A and B and θ^2 Ori A, with Na I absorption towards θ^2 Ori A also inferred.

In our own observations, many components are identified below a velocity of $\approx +15\,\mathrm{km\,s^{-1}}$ (see Fig. 4). In general, good agreement is seen between Na I and Ca II on a given sightline; however, less correlation is found between the Trapezium stars and θ^2 Ori A. These differences, coupled with the absence of similar components towards ι Ori, suggest the absorption to be arising in proximity to M42. The differences in cloud distributions between the Trapezium stars and θ^2 Ori A in this velocity range (echoed by the neutral lid absorption discussed in Section 7.1.1) again suggests θ^2 Ori A to be disconnected from the Trapezium stars. At the core of M42 is the Orion bar, a region of enhanced Hα emission running from the north-east to the south-west, passing between the Trapezium stars and θ^2 Ori A with a separation of only 30 arcsec from θ^2 Ori A. The bar is considered to be an ionization front viewed edge-on (Balick, Gammon & Hjellming 1974), again suggesting the presence of a transition in the line-of-sight absorption occurring between the Trapezium stars and θ^2 Ori A. A clear impression of the region may be gained from [O I] λ6300 imagery presented by Goudis (1982, p. 92, fig. 2.1.9, after Münch & Taylor 1974).

Many of the components with velocities less than $\approx +15\,\mathrm{km\,s^{-1}}$ are seen to be very broad, a signature of relatively high temperature and/or highly turbulent gas. However, the *b* values measured for many of these components imply temperatures in excess of 7000 K [about where collisional ionization of Na^0 is expected to become important Pottasch (1972)], suggesting possible unresolved substructure to be present. As pointed out by OD93, the second and third ionization energies of Ca are 11.9 and 50.9 eV, respectively, making Ca^{2+} the dominant ionization stage in the H II region. However, the high electron density in denser parts of the H II region (from H ionization) will enhance the recombination rate of Ca^{2+} to Ca^+, perhaps compensating for the higher photoionization rate. Similarly Na has first and second ionization energies of 5.1 and 47.3 eV, so that Na^+ will be the dominant ion stage of Na in H II regions as well as in neutral clouds. OD93 therefore suggest that either narrower lines, formed in a much cooler photodissociation region, or broader lines, arising within an ionized zone, may be observed. This being the case, many of the components seen in this velocity range could be due to secondary ionization fronts or the foreground H II region itself. The low Na^0/Ca^+ ratios suggest the gas to be disturbed, with Ca returned to the gas phase, while a poor correlation between sightlines is a signature of small-scale structure, neither of which would be unexpected for such a highly dynamic region of the ISM.

Absorption from He I 3889 Å arises from the metastable $2\,^3S$ state and is likely to come from the ionized zone. He I absorption components observed towards each of the Trapezium stars, at a radial velocity of $\approx$3 $\mathrm{km\,s^{-1}}$ (Oudmaijer et al. 1997; OD93), correspond reasonably well to the broad system M**5** towards θ Ori A and C (Fig. 4). Additional observation of θ^2 Ori A by OD93 suggests the He I absorption towards this star to be composed of two narrowly spaced components at ≈ -3 and $5\,\mathrm{km\,s^{-1}}$. This is echoed in our systems M**4** and M**6**. Although we detect a velocity shift of $\approx$3 $\mathrm{km\,s^{-1}}$ between our observations and those of He I, the very broad nature of the He I line shows this to be small. We therefore associate systems M**4**, M**5** and M**6** with foreground ionized gas, which according to the model of OD93 would be located on the near side of the neutral lid.

The components that constitute systems M**1** and M**11** show a large amount of variation between sightlines, making their association rather uncertain, and possibly indicating the absorption to arise in the M42 region. They have somewhat larger Na^0/Ca^+ ratios than observed for warm interstellar clouds. These systems possess velocities similar to the near and far ionization fronts identified by OD93 (3 and $12\,\mathrm{km\,s^{-1}}$ respectively), such that system M**1** may come from the near secondary ionization front, while system M**11** may be associated with the far secondary ionization front.

7.1.3 Foreground material

Spectra of ι Ori show the line of sight to this star to intersect far fewer absorbing clouds than those towards the θ^1 and θ^2 Ori stars. This is consistent with a location for ι Ori foreground to M42 (and the neutral lid), compatible with the view of OD93. It also suggests that the majority of the absorption detected towards the θ^1 and θ^2 Ori stars occurs in the vicinity of M42. Indeed, extended sightlines free from IS material are not uncommon.

Observations of ι Ori can be used to identify intervening absorbing material, such as the Na I and Ca II absorption of system M**7**, at a velocity of $\approx +8.4\,\mathrm{km\,s^{-1}}$. There is evidence that the Na I component is actually double, and it has been modelled as such; however, the Ca II counterpart can be (and has been) accurately modelled with a single component. OD93 associate this system [as seen in $\approx$8 $\mathrm{km\,s^{-1}}$ FWHM resolution observations made by Adams

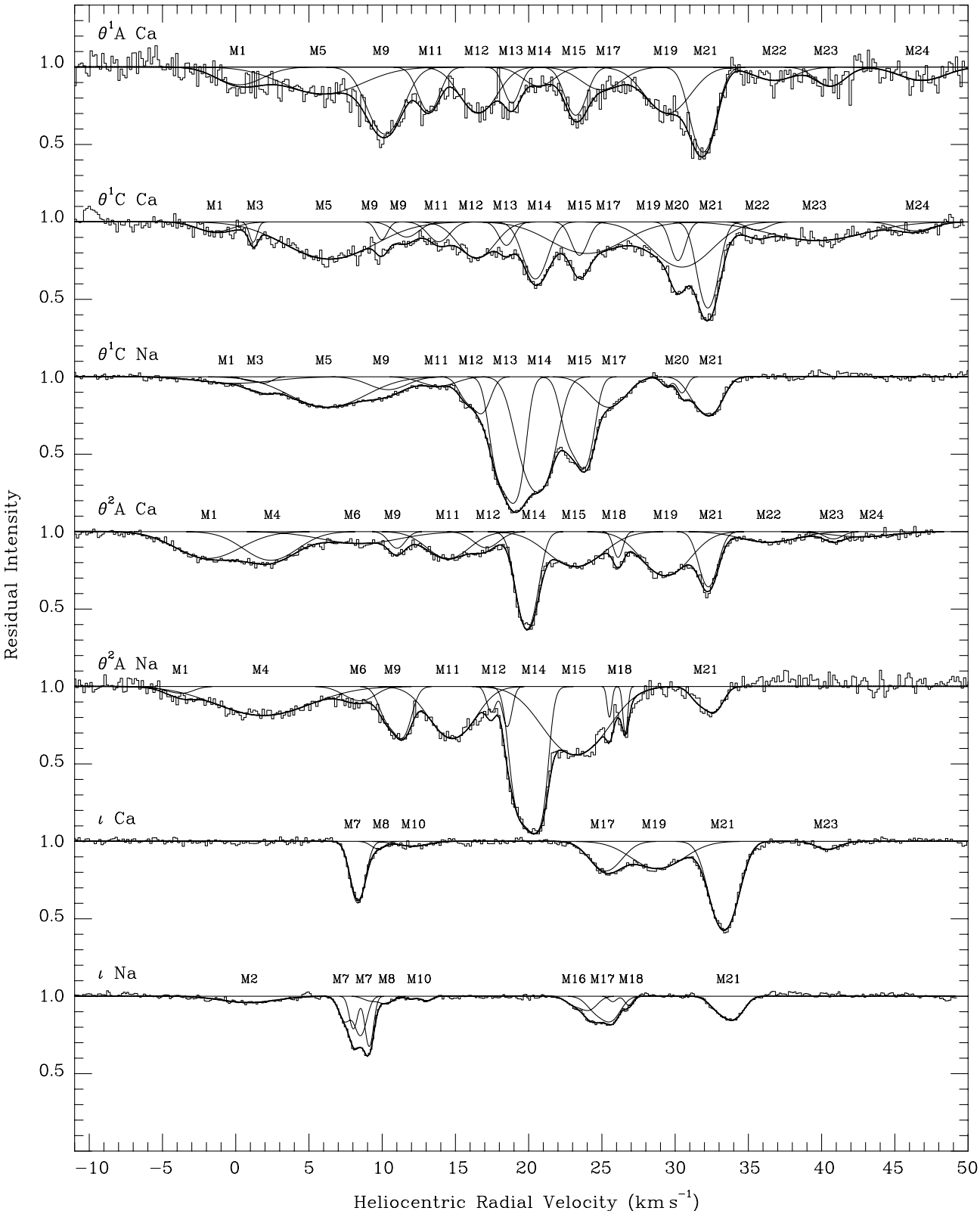

Figure 4. Absorption systems identified in the line of sight to the M42 region. Systems are numbered according to radial velocity and discussed in Section 7.1. The components that constitute systems **M1**, **M9** and **M11** show a large amount of variation between sightlines, making their identification somewhat uncertain. Where an identifier is given more than once for a given spectrum, each component is associated with the particular absorption system.

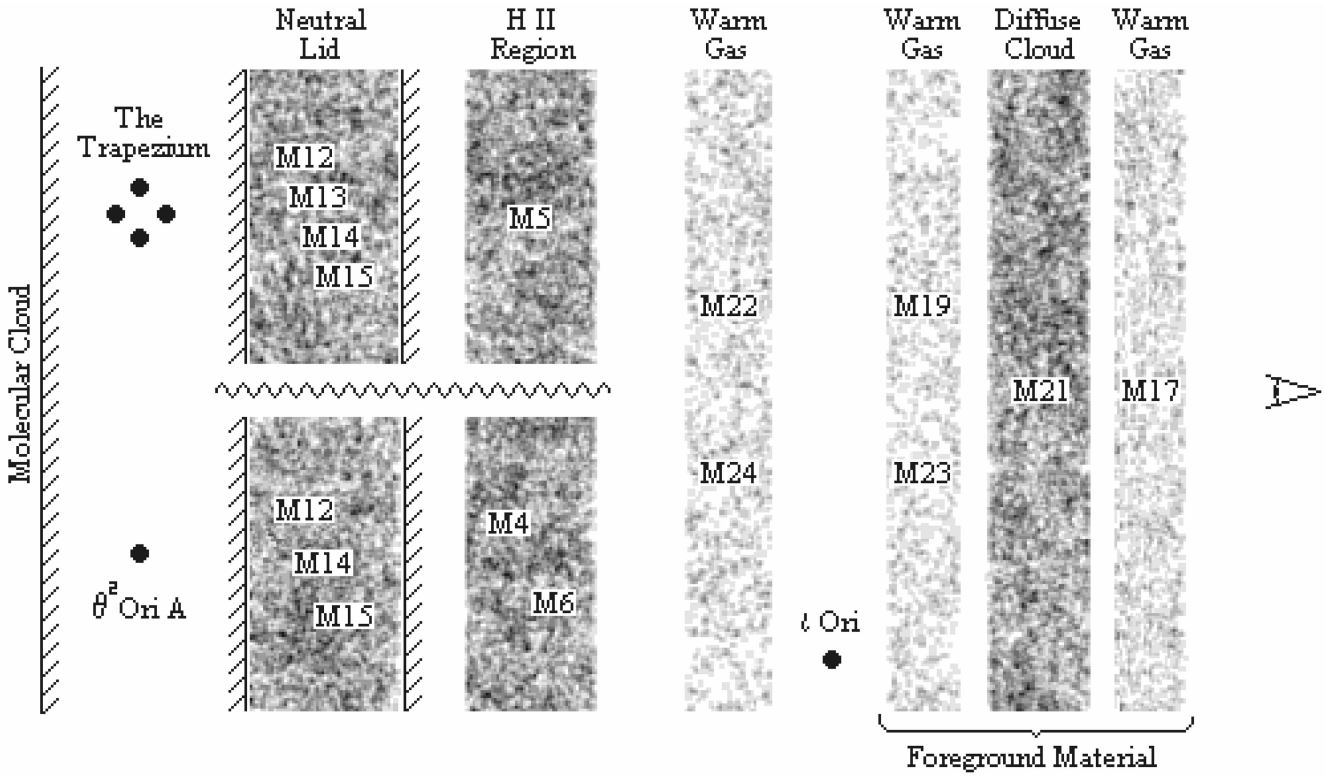

Figure 5. Line-of-sight velocity structure of the main absorption systems present in the direction of M42. Cloud boundaries marked with diagonal hatching are ionization fronts. The sinusoidal line represents a transition in the line-of-sight absorption occurring towards the Trapezium stars and θ^2 Ori (see e.g. fig. 1 of Peimbert 1982). For simplicity, systems M**22** and M**24** and systems M**19** and M**23** are shown to be present in the same region – however, they are not necessarily associated. System M**17** is located within 75 pc of the Sun, while all other systems are beyond 75 pc. ι Ori is located ≈40 pc foreground to the Trapezium stars. Angular separations between θ^1 Ori A and θ^1 Ori C, θ^2 Ori A and ι Ori project to linear distances (at M42) of 0.03 pc, 0.3 pc and 4 pc, respectively.

(1944)] with absorption centred at $+6.8\,\mathrm{km\,s^{-1}}$ on the neighbouring sightlines to the more distant θ^1 Ori stars. In this study we find the absorption collected together by OD93 in their $+6.8\,\mathrm{km\,s^{-1}}$ system to be composed of components with an array of linewidths and column densities, over a range of velocities. We can make a tentative connection between the foreground system M**7** and system M**9**. The overall Na^0/Ca^+ ratio of system M**9** is 3.1 (1.2 towards θ^1 Ori C; 7.1 towards θ^2 Ori A), larger than generally measured for the systems below a velocity of $\approx +15\,\mathrm{km\,s^{-1}}$ (largely attributed to absorption arising within a foreground H II region; see Section 7.1.2), suggesting that the absorption may not be associated with the M42 region.

Systems M**8** and M**10** are only detected towards ι Ori. The very weak nature of both systems means that they would be difficult to detect in the more complex spectra of the other stars.

Two other weak Na I components are detected in the spectrum of ι Ori, those of systems M**16** and M**18**. In the case of system M**16**, corresponding components are rendered undetectable in the spectra of other M42 stars because of the much stronger neutral lid absorption at these velocities. In the case of system M**18**, an association can be made with narrow Na I and Ca II components seen towards θ^2 Ori A but undetected towards the remaining stars.

System M**17** is not detected towards θ^2 Ori A, but is observed towards each of the other stars in both Na I and Ca II. Its absence from the spectrum of θ^2Ori A may be the result of a significant amount of blending with the neighbouring (in velocity space) neutral lid components (discussed in Section 7.1.1). System M**17** is characterized by fairly broad components with a low Na^0/Ca^+ ratio. This suggests that the absorption arises in warm gas, thereby maintaining a significant amount of gas-phase Ca. Observations of γ Ori, which is located 12° away on the sky and at a *Hipparcos* distance of only 75 pc (ESA 1997), have been made in Na I (Welsh et al. 1990), revealing one component at a velocity of $+25.8\,\mathrm{km\,s^{-1}}$, but revealing four components between +15 and $+30\,\mathrm{km\,s^{-1}}$ in Ca II (Vallerga et al. 1993). Comparison of these components with those seen in our UHRF data suggests that system M**17** arises in the same cloud seen towards this foreground star, thus locating the system within 75 pc of the Sun.

System M**19** shows up as Ca II absorption seen towards each of the targets, although we note that the parameters characterizing the component towards θ^1 Ori C appear to give larger values of $v_\odot$, b and N compared to corresponding components in the other sightlines/ions. The broad nature of this system, coupled with its very low Na^0/Ca^+ ratio, means that the absorption is likely to arise in foreground warm intercloud medium.

System M**21** can be confidently classed as a foreground diffuse cloud. Its constituent components exhibit excellent agreement between all the sightlines. The system is composed of relatively narrow components and possesses a fairly small mean Na^0/Ca^+ ratio (≈0.6). The absence of similar absorption in the spectrum of the foreground star γ Ori signifies that the cloud is likely to be located beyond a distance of 75 pc. We note that it has a relatively high radial velocity and feel that it is the main constituent of OD93's $+31\,\mathrm{km\,s^{-1}}$ system.

Above a velocity of $\approx +35\,\mathrm{km\,s^{-1}}$, only Ca II absorption is detected, consistent with the findings of Routly & Spitzer (1952),

Table 6. Velocity systems identified towards the λ Ori association. The first row lists the system identifiers, as referred to in the text. In the next rows, a short description is given for some of the systems, with $\bar{v}_{\odot}$ being the mean velocity of the constituent components. The last two rows list the numbers of the clouds observed towards λ and ϕ^1 Ori (as given in Table 3), which are contained in each system.

System		**λ1**	**λ2**	**λ3**	**λ4**	**λ5**	**λ6**	**λ7**	**λ8**	**λ9**	**λ10**	**λ11**	**λ12**
Description		Material accelerated by λ Ori	WISM similar to Belt stars	Cool gas	WISM similar to Belt stars	λ Ori shell material	Cold diffuse molecular cloud				Foreground diffuse molecular gas		
Velocity, $\bar{v}_{\odot}$		−19	−9	−6	−2	+7	+10	+15	+18	+20	+25	+30	+33
Cloud:	λ	1	2	3	4	5,6,8	7	9	10	11	12	13	14
	ϕ^1		1		2	3		4	5	6	7,8		

whereby smaller Na^0/Ca^+ ratios are found at larger absolute LSR velocities. Systems M**22** and M**24** are observed towards θ^1 Ori A and C and θ^2 Ori A, and are thus likely to be located between ι Ori and the Trapezium stars, while system M**23** is also observed towards ι Ori and is thus located in the foreground. Owing to their generally broad nature, and the lack of associated Na I absorption, each of these systems is likely to arise in the warm intercloud medium. These three systems comprise OD93's $+39\,km\,s^{-1}$ system, which they inferred to have associated Na I absorption in the case of θ^1 Ori C. However, as discussed in Section 4.5, we believe that this putative Na I component is likely to be telluric absorption in the original spectra of Hobbs (1978b).

7.1.4 Remaining components

System M**2**, observed towards ι Ori, is unusual in that it consists of a very broad Na I component with no associated Ca II detectable here. The observations reported by W94 echo the detection of Na I, while those of W96 show associated weak Ca II absorption also to be present at this velocity. Although rather weaker, this system bears some resemblance to system M**4**, observed towards θ^2 Ori A (discussed in Section 7.1.2), and highlights the possibility that some of the absorption at this velocity may occur in the foreground, rather than being wholly associated with M42. Under the assumption of zero turbulence, this component is found to have a kinetic temperature of $\approx 10^4$ K, perhaps indicating the presence of highly blended substructure.

System M**3**, only observed towards θ^1 Ori C, is composed of narrow components in both Na I and Ca II, indicative of cold absorbing gas. Under the assumption of no internal cloud turbulence, a rigorous upper limit of 312 K can be placed on the kinetic temperature of the Ca^+ absorbers. This may indicate that the absorption arises in a compact knot of material small enough not to intersect neighbouring sightlines

System M**20** is blended between systems M**19** and M**21** and has only been confidently identified towards θ^1 Ori C where narrow components are observed in both Na I and Ca II. Possible asymmetry in system M**21** absorption towards θ^1 Ori A suggests that there may also be a counterpart present towards this star as well. No corresponding absorption is seen towards θ^2 Ori A, thus locating system M**20** over the face of the Trapezium.

7.2 The λ Orionis association

Observations and model fits for λ Ori and ϕ^1 Ori are presented here. Through the comparison of Ca II and Na I absorption occurring in the sightlines to λ and ϕ^1 Ori, separate absorption systems have been identified and are listed in Table 6. System identifiers are of the form **λ*x***, where 'λ' denotes 'λ Ori association' (in order to reduce confusion with individual clouds), and ***x*** is a number that increases with the system's mean central velocity. A more detailed analysis will be presented elsewhere (Price et al. in preparation), utilizing additional lower-resolution ($R = 110000$) observations of a number of targets with locations in and around the λ Ori association.

The O8III star λ Orionis is located at the centre of the spherically symmetric H II region S264 (Sharpless 1959), making it a good example of a classical Strömgren sphere. S264 is in a state of expansion (Mathews 1965; Lasker 1966) and is interior to expanding rings of molecular gas and dust (Maddalena & Morris 1987; Zhang et al. 1989). Also located within the boundaries of S264 is the B0IV star ϕ^1 Orionis whose angular separation of 27 arcmin projects to a linear distance of ≈2.5 pc at the distance of the association (Table 1). Their similar location is reflected in their similar IS spectra.

The molecular gas, observed in CO, is some 10° in diameter (Maddalena & Morris 1987), or ≈57 pc if we adopt a distance to λ Ori of 324 pc (Table 1). Kinematical models of this ring constructed by Maddalena & Morris suggest it to have a central radial velocity of $+21.2\,km\,s^{-1}$, to be tilted by 36.4° to the line of sight, and to be expanding at a rate of $14.3\,km\,s^{-1}$. Its present size and velocity suggest that its expansion started 2.4×10^6 yr ago, consistent with an estimated age for λ Ori of 2–4 Myr (Murdin & Penston 1977).

While not coincident with the molecular emission, the dust ring seen by *IRAS* appears well defined, less elliptical and centred on λ Ori (Zhang et al. 1989). As argued by Zhang et al. (1989), on the grounds of energy input, the ring-like appearance is quite probably the result of a projection effect of a shell (radius ≈30 pc, thickness ≈1 pc) since the outer edges of a shell, viewed tangentially, will possess column densities more readily observable than those seen radially. If the gas and dust were in the form of rings (not intersected by the line of sight), no detectable absorption would be produced in the spectra of the central stars, contrary to the observed strong absorption seen in Ca II and Na I towards λ and ϕ^1 Ori, discussed below. The powerful stellar wind generated by λ Ori once it reached the main sequence is believed to have produced a shell of swept-up material. According to Bergoffen & Van Buren (1988), during the early stages of the expansion, the shock velocity should have been sufficient to remove material from grain surfaces. Therefore gas present in the shell should exhibit lower Na^0/Ca^+ ratios.

The Na I absorption seen by H69 at +16.8 and $+25.8\,km\,s^{-1}$ towards λ Ori is considered by Maddalena & Morris (1987) to

reside at velocities consistent with the near and far sides of the shell, placing λ Ori behind the shell, rather than within it. However, since Maddalena & Morris derived central radial and expansion velocities of +21.2 and +14.3 km s^{-1} for the ring, the material on the near and far sides of the shell (if its expansion were to follow that of the ring) should be found at +7 and +36 km s^{-1} respectively, rather than at the velocities suggested by Maddalena & Morris. A lack of absorption at a velocity of +36 km s^{-1} (corresponding to the velocity of the far side of the shell) suggests that λ and ϕ^1 Ori indeed reside within the shell, as would be expected.

The very strong Ca II absorption observed between +4 and +11 km s^{-1} (system **λ5**), towards both λ and ϕ^1 Ori, corresponds well to the velocity implied for the near side of a shell around the association by the kinematic model of Maddalena & Morris (1987). Moreover, the small Na^0/Ca^+ ratios are consistent with the expected removal of Ca from grain surfaces (Bergoffen & Van Buren 1988). We therefore consider this absorption to arise within the near side of the expanding shell around the association. 23 Ori, which is located at a similar distance but exterior to the λ Ori shell on the sky, has a similar Ca II spectrum, but does not exhibit strong absorption at a radial velocity of ≈ +7 km s^{-1} (Welty et al. 1999), strengthening our conclusion for its origin being from a neutral shell around the λ Ori association.

We suggest that the very narrow components of system **λ6** (characteristic of very cold gas; $T_k < 117$ K in the case of Na I) corresponds well to molecular hydrogen absorption observed by Spitzer & Morton (1976), and arises within a particularly dense IS cloud. Although highly blended with neighbouring components, these components form an integral part of an absorption model that statistically provides the best fit to the data. Furthermore, excellent agreement is seen between the independently modelled Na I and Ca II data.

The components present at negative velocities also possess very small Na^0/Ca^+ ratios. System **λ1**, which is only observed towards λ Ori, possesses a velocity more negative than any other cloud (apart from absorption associated with mass loss from β Ori, see Section 7.4). System **λ1** may be associated with, and accelerated by, λ Ori. Good agreement is seen between λ and ϕ^1 Ori for systems **λ2** and **λ4**. Their broad nature and low Na^0/Ca^+ ratios are consistent with the gas either being shocked material associated with the λ Ori shell and accelerated by association stars, or being in the warm intercloud medium, known to exhibit larger velocity ranges than diffuse clouds (Cowie & York 1978). The detection of similar components in the Ca II spectra of the Belt stars suggests the latter case to be more likely. The weak absorption of system **λ3** seen towards λ Ori is not detectable in the spectrum of ϕ^1 Ori.

The location of λ Ori's saturated Na I absorption around +25.7 km s^{-1} corresponds well with its counterpart in the spectrum of ϕ^1 Ori. These saturated regions can be accurately fitted with single components (which will have no unique solution for b and N) but are undoubtedly the result of unresolved blends. This is supported by the following considerations: (i) the identification of six Ca II components in this velocity region of the λ Ori spectrum; (ii) the unsaturated red wing towards ϕ^1 Ori, which requires a minimum of two components for an accurate fit; and (iii) the requirement of an additional component in the blue wing for λ Ori. However, since it is not possible to identify individual IS clouds, this region is treated as a single absorption system, **λ10**. The total column densities of Na^0 and Ca^+ indicate Na^0/Ca^+ ratios of 13.49 and 7.19 for λ and ϕ^1 Ori respectively (see Section 6), consistent with cool diffuse/partially molecular clouds (since Ca depletion is expected to be density dependent; e.g. Barlow 1978). This is supported by the observation of an H_2 absorption component at a velocity of +25.4 km s^{-1} towards λ Ori (Spitzer & Morton 1976).

Relatively weak absorption from both Na I and Ca II is observed – by Welsh et al. (1990) and Vallerga et al. (1993) respectively – at ≈+26 km s^{-1} in the spectrum of γ Ori, 4° distant, a velocity corresponding to the saturated region of λ and ϕ^1 Ori. γ Ori is a foreground star, with a *Hipparcos* distance of only 75 pc (ESA 1997). This suggests that, while a small proportion of the absorption in the saturated region may occur within 75 pc of the Sun, the majority originates beyond this distance.

7.3 The Belt region

Orion's Belt is composed of the three bright supergiant stars (from west to east) δ, ε and ζ Ori. Also discussed in this section is the O9.5V star σ Ori, located 50 arcmin to the south of ζ Ori (projecting to a linear separation of 3 pc at a distance of 300 pc) and responsible for sculpting the Horsehead nebula. The Horsehead is found to have a radial velocity of +28 km s^{-1} (Milman et al. 1975), and is located 35 arcmin to the east of σ Ori. The destructive UV radiation from the σ Ori system produces the ionization of the H II region IC 434, against which the Horsehead appears in silhouette [see fig. 5.1.1 of Goudis (1982) for a map of the region]. ζ Ori is located on the western edge of the Orion B cloud and, although very close on the sky to the nebula NGC 2024 (Orion B), it is thought to be in the foreground (at a distance of ≈250 pc, Table 1), and not to play a significant part in its ionization (Goudis 1982). The interstellar absorption towards both δ and ζ Ori has been found to exhibit temporal variability, as discussed in Section 4.

With the exception of δ Ori, each of these stars exhibits strong Na I absorption, with generally large Na^0/Ca^+ ratios, around a velocity of +25 km s^{-1}. In each case the absorption is found to be complex, and split into two separate systems. Although the Na I absorption towards ε Ori is blended into a single multicomponent feature, the weaker Ca II lines clearly show the presence of two features. Corresponding absorption in K I (ε and ζ Ori) and in molecular hydrogen at these velocities (Spitzer & Morton 1976; Jenkins & Peimbert 1997; Jenkins et al. 2000), coupled with the large Na^0/Ca^+ ratios, leads to the conclusion that this absorption is due to foreground cool, diffuse clouds containing a small amount of molecular material. The broad similarities between these sightlines are consistent with the presence of an inhomogeneous layer of material overlying the area as a whole, the radial velocity of which is in agreement with that of the Orion–Eridanus shell (Brown et al. 1995).

Additional strong, narrow Na I absorption is also observed towards ε and ζ Ori at lower velocities. Similar components are not generally seen towards the other Orion stars and are possibly only associated with the Belt region. The strongest of these is cloud 5 towards ε Ori at a velocity of ≈ +11 km s^{-1}. However, the H I observations by Brown et al. (1995) do not rule out the presence of Orion–Eridanus shell material at these velocities in these sightlines.

H I observations made by Chromey, Elmegreen & Elmegreen (1989) show the presence of an expanding shell in the Belt region, centred around σ Ori. The near and far sides of the σ Ori shell possess radial velocities of ≈ +22 and +37 km s^{-1}, respectively, although the exact locations of the stars with respect to the shell are not known. Chromey et al. (1989) propose the shell material to be partially molecular, suggesting that some of the strong absorption

that we observe around $+25\,\mathrm{km\,s^{-1}}$ possibly arises in the near side of this shell. The velocity of the shell's far side coincides with the absorption seen around $+37\,\mathrm{km\,s^{-1}}$ towards each of the Belt stars (discussed below). However, the low Na^0/Ca^+ ratios measured for this absorption are not consistent with molecular gas, and this suggests that the stars lie within or in the foreground to the shell. In this case, the broad Ca II absorption observed at a velocity of $\approx+37\,\mathrm{km\,s^{-1}}$ towards each of these four stars can be considered to arise from warm intercloud medium material. Although not detected towards δ Ori in our low-S/N Ca II observation, absorption can be seen at this velocity in the lower-resolution but higher-S/N observation of W96. This system may be associated with the similar absorption observed towards the M42 region (system M**23**, Section 7.1.3).

The lowest-velocity broad Ca II absorption seen towards the Belt stars is also thought to originate from the warm intercloud medium. However, in the case of the sightline towards ζ Ori, Jenkins & Peimbert (1997) have inferred the presence of a standing bow shock using observations of H_2. Shifts in both the central velocity, and broadening detected for absorption from successive rotational levels of the H_2 molecule, are interpreted as being the result of H_2 forming in two separate regions behind the standing bow shock (Jenkins & Peimbert 1997). Absorption from the lower rotational levels is considered to arise in cold, compressed gas (where H_2 is formed via grain surface reactions), while that from higher rotational levels is thought to come from much warmer gas closer to the shock front (where H_2 is produced through gas-phase reactions).

The H_2 absorption arising from the lower rotational levels ($J = 0$ and 1) corresponds well with our observation of cold (variable) Na I and K I absorption, cloud 2e†. The temperature–turbulence analysis performed on this cloud in Section 5 using Na I and K I components has shown the upper limit of T_k to be 293 K, very similar to the upper limit that can be calculated from the corrected (cf. footnote b, table 6 of Jenkins & Peimbert 1997) broadening of H_2 ($J = 0$), which yields $T_\mathrm{k} < 289$ K. If the Na I and H_2 absorption is indeed occurring from the same region, a temperature–turbulence analysis (as described in Section 5) shows $1 < T_\mathrm{k} < 289$ K while $0.02 < v_\mathrm{t} < 0.32\,\mathrm{km\,s^{-1}}$. Similarly, H_2 absorption from the higher rotational levels ($J = 2$ to 5), which Jenkins & Peimbert attribute to gas with $T_\mathrm{k} = 6500$ K, corresponds well with the broader Na I and Ca II components of our cloud 2c.

7.4 β Orionis

With $V = 0.28$, the B8Ia star β Orionis (Rigel) is the brightest star in the constellation. β Ori is located at the western foot of Orion, just beyond the confines of Barnard's Loop. The presence of strong photospheric Ca II absorption has created some uncertainty as to the location of the continuum level (noted in Section 2), and therefore the true IS absorption contribution.

Numerous studies have revealed β Ori to be undergoing mass loss ($\dot{M} \approx 1.1 \times 10^{-6}\,\mathrm{M_\odot\,yr^{-1}}$; e.g. Barlow & Cohen 1977), while Hα observations made by Israelian, Chentsov & Musaev (1997) have detected both the outflow and infall of material, at a range of velocities, interpreted by those authors as moving through closed magnetic loops around β Ori. The Ca II spectrum observed towards β Ori (Fig. 1) is rather unusual in that it exhibits strong absorption out to a velocity of $-35\,\mathrm{km\,s^{-1}}$. With a stellar radial velocity of $+20.7\,\mathrm{km\,s^{-1}}$ (Wilson 1953), these components have outflow velocities of up to $55\,\mathrm{km\,s^{-1}}$ with respect to β Ori, and are likely to be a result of the ongoing mass loss. The very low Na^0/Ca^+ ratios measured for the Ca II components below a velocity of $-10\,\mathrm{km\,s^{-1}}$ support a circumstellar origin. Furthermore, the linewidths characterizing the optimized Ca II model components imply gas with temperatures (under the assumption of zero turbulence) of $1200\,\mathrm{K} < T_\mathrm{k} < 8200\,\mathrm{K}$.

Although the absorption components at ≈0 and $+10\,\mathrm{km\,s^{-1}}$ may arise in either the warm interstellar medium or the circumstellar environment of β Ori, the unusually strong, discrete appearance of the components, coupled with possible variability (discussed in Section 4.7), argues for a circumstellar origin.

The Na I spectrum of β Ori also appears to be somewhat unusual, reaching only ≈0.8 of the continuum intensity (although it should be noted that β Ori also possesses the weakest Ca II K absorption of the stars observed), while sightlines towards ζ and κ Ori (located at similar distances) exhibit much stronger absorption. Between velocities of +15 and $+25\,\mathrm{km\,s^{-1}}$, each Na I component is found to possess larger Na^0/Ca^+ ratios (≈10), consistent with an origin within diffuse IS clouds, where Ca is depleted on to grain surfaces. For example, the cold ($T_\mathrm{k} < 67$ K) Na I component at $+18.85\,\mathrm{km\,s^{-1}}$, although close to a broader neighbouring component ($v_\odot = +18.40\,\mathrm{km\,s^{-1}}$), displays clear hyperfine splitting (HFS) with little or no associated Ca II absorption. Although broader, and possibly the result of a blend of narrower lines, Na I component 9 also possesses little or no associated Ca II absorption.

Detected in Ca II, cloud 15 possesses little or no associated Na I absorption and is located at a velocity of $+29.12\,\mathrm{km\,s^{-1}}$ (i.e. travelling towards β Ori). This cloud is therefore likely to have an interstellar origin, within the warm intercloud medium, rather than the circumstellar environment.

7.5 κ Orionis

κ Ori is located at the southern tip of the Orion A cloud, which is part of the southern molecular cloud complex and outside the confines of Barnard's Loop. Observations of both Na I and K I have been obtained for this star. Parameters derived from absorption-line modelling of the available data have been used in Section 5 to derive limits on T_k and v_t for four clouds. Ca II observations of κ Ori were obtained by W96 at a resolution of $1.20\,\mathrm{km\,s^{-1}}$ FWHM, and comparisons with our Na I and K I observations indicate the absorption towards this star to be contained within three broad velocity bands.

Below a velocity of $+10\,\mathrm{km\,s^{-1}}$, W96 detect six broad Ca II components, three of which are present at velocities corresponding to Na I components detected here. The radial velocities of these components render the clouds blueshifted with respect to κ Ori by between 12 and $30\,\mathrm{km\,s^{-1}}$. These components may arise from shell material around κ Ori. The measured Na^0/Ca^+ ratios are seen to be lower for absorption at larger negative velocities. An H_2 component observed at $+1.7\,\mathrm{km\,s^{-1}}$ by Spitzer & Morton (1976) indicates some of the absorption in this blended region to arise in relatively dense gas.

The very strong Na I absorption present between +15 and $+25\,\mathrm{km\,s^{-1}}$ is associated with little Ca II absorption, generating much larger Na^0/Ca^+ ratios. Observations of H I by Hobbs (1971) show very strong 21-cm emission around $+20\,\mathrm{km\,s^{-1}}$, while the observations of Spitzer & Morton (1976) indicate some absorption from molecular hydrogen to be present at this velocity and possibly $+24\,\mathrm{km\,s^{-1}}$. This suggests these components

to be the result of diffuse clouds with some associated molecular material.

While we have not detected Na I absorption above a velocity of $+25\,\mathrm{km\,s^{-1}}$, W96 identify four broad Ca II components at these more positive radial velocities, characteristic of warm, intercloud gas.

8 CONCLUSIONS

The main conclusions of this paper are as follows:

(i) The data presented here represent the highest-resolution interstellar line observations obtained for many of the targets. Our observations of stars located within the Orion nebula (a region not previously studied at such high resolution) have revealed two or three times as many absorption components as previously identified by Hobbs (1978b), OD93 and W96. Our ultra-high-resolution data have thus enabled a much more accurate perspective to be obtained of the absorbing medium in this direction, and highlight the necessity for ultra-high-resolution, high-S/N observations when studying the diffuse ISM.

(ii) Where a cloud has been observed in both Na I and K I (expected to exist co-spatially), the line broadening produced by each species has been used to determine the kinetic temperature and line-of-sight rms turbulent velocity (Section 5). In all cases, we find that turbulent motions are almost certainly subsonic.

(iii) The UHRF data have enabled the identification of many individual interstellar clouds, for which Na^0/Ca^+ ratios have been obtained (Section 6). An examination of these Na^0/Ca^+ ratios provides an indication of the physical conditions prevailing within each cloud, and shows the presence of distinct groups, which are utilized in the analysis of the ISM in this direction.

(iv) Overall, we detect a small velocity gradient in the location of strong Na I absorption over the region (discussed in Section 6). This is consistent with this absorption arising in the neutral gas marking the boundary of the Orion–Eridanus superbubble, which shows a similar trend in H I observations made by Brown et al. (1995, cf. their fig. 8).

(v) Observations of closely spaced targets in the M42 region (Section 7.1) and λ Ori association (Section 7.2) have been used to discern the line-of-sight velocity structure. Differences in the line-of-sight absorption occurring in sightlines with small angular separations has highlighted the presence of small-scale structure in the ISM on a variety of spatial scales (down to 5800 au in the case of θ^1 Ori A and C). Furthermore, the comparison of our observations with earlier work (Section 4) has illustrated several examples of temporal line-profile variability, also adding to evidence that small-scale structure is ubiquitous in the ISM (down to 7 au in the case of cloud 2e† towards ζ Ori).

ACKNOWLEDGMENTS

We thank PATT for the award of telescope time. RJP and IAC thank PPARC for the award of a Research Studentship and an Advanced Fellowship, respectively. We also wish to thank the referee, Professor Steven Federman, for helpful comments on the original manuscript.

REFERENCES

Adams W. S., 1944, PASP, 56, 119
Balick B., Gammon R. H., Hjellming R. M., 1974, PASP, 86, 616
Bally J., Langer W. D., Wilson R. W., Stark A. A., Pound M. W., 1990, in Falgarone E., Boulanger F., Dutert G., eds, Proc. IAU Symp. 147, Fragmentation of Molecular Clouds and Star Formation. Kluwer, Dordrecht, p. 11
Barlow M. J., 1978, MNRAS, 183, 417
Barlow M. J., Cohen M., 1977, ApJ, 213, 737
Barlow M. J., Silk J., 1977, ApJ, 211, 83
Barlow M. J., Crawford I. A., Diego F., Dryburgh M., Fish A. C., Howarth I. D., Spyromilio J., Walker D. D., 1995, MNRAS, 272, 333
Barnard E. E., 1895, Pop. Astron., 2, 151
Beals C. S., 1936, MNRAS, 96, 661
Bergoffen M. J., Van Buren D., 1988, AJ, 95, 130
Black J. H., van Dishoeck E. F., 1988, ApJ, 331, 986
Brown A. G. A., Hartmann D., Burton W. B., 1995, A&A, 300, 903
Chromey F. R., Elmegreen B. G., Elmegreen D. M., 1989, AJ, 98, 2203
Conti P. S., Alschuler W. R., 1971, ApJ, 170, 325
Cowie L. L., Songaila A., 1986, ARA&A, 24, 499
Cowie L. L., Songaila A., York D. G., 1979, ApJ, 230, 469
Cowie L. L., York D. G., 1978, ApJ, 223, 876
Crawford I. A., 1992, MNRAS, 259, 47
Crawford I. A., 1995, MNRAS, 277, 458
Crawford I. A., Barlow M. J., Blades J. C., 1989, ApJ, 336, 212
Deutschman W. A., Davis R. J., Schild R. E., 1976, ApJS, 30, 97
Diego F., 1993, Appl. Opt., 32, 6284
Diego F. et al., 1995, MNRAS, 272, 323
Dunkin S. K., Crawford I. A., 1999, MNRAS, 302, 197
ESA, 1997, The Hipparcos and Tycho Catalogues, ESA SP-1200. ESA Publications Division, Noordwijk
Evans D. S., 1967, in Batten A. H., Heard J. F., eds, Proc. IAU Symp. 30, Determination of Radial Velocities and their Applications. Academic Press, London, p. 57
Federman S. R., 1982, ApJ, 257, 125
Goudis C., 1982, The Orion Complex: A Case Study of Interstellar Matter. Dordrecht, Reidel
Hartmann J., 1904, ApJ, 19, 268
Heiles C. et al., 1999, in Taylor A. R., Landecker T. L., Joncas G., eds, ASP Conf. Ser. Vol. 168, New Perspectives on the Interstellar Medium. Astron. Soc. Pac., San Francisco, p. 211
Hobbs L. M., 1969a, ApJ, 157, 135 (H69)
Hobbs L. M., 1969b, ApJ, 157, 165
Hobbs L. M., 1969c, ApJ, 158, 461
Hobbs L. M., 1971, ApJ, 166, 333
Hobbs L. M., 1973, ApJ, 181, 79
Hobbs L. M., 1978a, ApJ, 222, 491
Hobbs L. M., 1978b, ApJS, 38, 129
Hobbs L. M., Welty D. E., 1991, ApJ, 368, 426
Hoffleit D., Jaschek C., 1982, The Bright Star Catalogue, 4th edn. Yale Univ. Observatory, New Haven, CT
Howarth I. D., Murray J., Mills D., 1993, Starlink User Note No. 50
Israelian G., Chentsov E., Musaev F., 1997, MNRAS, 290, 521
Jenkins E. B., Peimbert A., 1997, ApJ, 477, 265
Jenkins E. B., Woźniak P. R., Sofia U. J., Sonneborn G., Tripp T. M., 2000, ApJ, 538, 275
Jura M., 1976, ApJ, 206, 691
Lambert D. L., Danks A. C., 1986, ApJ, 303, 401
Lasker B. M., 1966, ApJ, 143, 700
Lauroesch J. T., Meyer D. M., Blades J. C., 2000, ApJ, 543, 43
Maddalena R. J., Morris M., 1987, ApJ, 323, 179
Marschall L. A., Hobbs L. M., 1972, ApJ, 173, 43
Mathews W. G., 1965, ApJ, 142, 1120
Milman A. S., Knapp G. R., Kerr F. J., Knapp S. L., 1975, AJ, 80, 93
Morgan W. W., Code A. D., Whitford A. E., 1955, ApJS, 2, 41
Morton D. C., 1991, ApJS, 77, 119
Münch G., Taylor K., 1974, ApJ, 192, 93
Murdin P., Penston M. V., 1977, MNRAS, 181, 657
O'Dell C. R., Valk J. H., Wen Z., Meyer D. M., 1993, ApJ, 403, 678 (OD93)
O'Dell C. R., Wen Z., 1992, ApJ, 387, 229

Oudmaijer R. D., Drew J. E., Barlow M. J., Crawford I. A., Proga D., 1997, MNRAS, 291, 110
Peimbert M., Ann N. Y., 1982, Acad. Sci., 395, 24
Phillips A. P., Pettini M., Gondhalekar P. M., 1984, MNRAS, 206, 337
Pickering W. H., 1890, Siderial Messenger, 9, 2
Pottasch S. R., 1972, A&A, 20, 245
Price R. J., Crawford I. A., Barlow M. J., 2000, MNRAS, 312, L43 (Paper I)
Price R. J., Crawford I. A., Howarth I. D., 2001, MNRAS, 321, 553 (Paper II)
Reynolds R. J., Ogden P. M., 1979, ApJ, 229, 942
Routly P. M., Spitzer L., Jr, 1952, ApJ, 115, 227
Savage B. D., Bohlin R. C., Drake J. F., Budich W., 1977, ApJ, 216, 291
Sharpless S., 1959, ApJS, 4, 257
Shortridge K. et al., 1999, Starlink User Note, No. 86.17
Spitzer L., Jr., 1978, Physical Processes in the Interstellar Medium. John Wiley, New York, p. 216–17
Spitzer L., Jr, Morton W. A., 1976, ApJ, 204, 731
Vallerga J. V., Vedder P. W., Craig N., Welsh B. Y., 1993, ApJ, 411, 729
van der Werf P. P., Goss W. M., 1989, A&A, 224, 209
Warren W. H., Hesser J. E., 1978, ApJS, 36, 497
Welsh B. Y., Vedder P. W., Vallerga J. V., 1990, ApJ, 358, 473
Welty D. E., Hobbs L. M., 2001, ApJS, 133, 345 (W01)
Welty D. E., Hobbs L. M., Kulkarni V. P., 1994, ApJ, 436, 152 (W94)
Welty D. E., Morton D. C., Hobbs L. M., 1996, ApJS, 106, 533 (W96)
Welty D. E., Hobbs L. M., Lauroesch J. T., Morton D. C., Spitzer L., York D. G., 1999, ApJS, 124, 465
Wen Z., 1993, PhD thesis, Rice Univ.
Wilson R. E., 1953, General Catalogue of Stellar Radial Velocities, Carnegie Inst. Publ. 601. Carnegie Inst., Washington, DC
Zhang C. Y., Laureijs R. J., Chlewicki G., Clark F. O., Wesselius P. R., 1989, A&A, 218, 231
Zuckerman B., 1973, ApJ, 183, 863

This paper has been typeset from a TEX/LATEX file prepared by the author.